5-2023

Impacts of Preferential Flow on Tc-99and Np-237 Vadose Transport in Soils at the Savannah River Site

Josh Parris
jparri3@clemson.edu

IMPACTS OF PREFERENTIAL FLOW ON Tc-99 AND Np-237 VADOSE TRANSPORT IN SOILS AT THE SAVANNAH RIVER SITE

A Thesis
Presented to
the Graduate School of
Clemson University

In Partial Fulfillment
of the Requirements for the Degree
Master of Science
Hydrogeology

by
Joshua Luke Parris
May 2023

Accepted by:
Dr. Brian Powell, Committee Chair
Dr. Lawrence Murdoch
Dr. Christophe Darnault

ABSTRACT

Since the 1950s, the United States has produced approximately 90,000 metric tons of spent nuclear fuel (SNF) (Office of Nuclear Energy, 2022); however, no long-term storage solutions are available. Technecium-99 and neptunium-237, two fission products found in SNF, readily form highly mobile species in oxidizing conditions (Hu, 2008; Bondietti, 1979) and have respective half-lives of 2.13×10^5 and 2.14×10^6 years (Hu, 2010). Considering these characteristics, ^{99}Tc and ^{237}Np are two risk-driving isotopes found in SNF storage. The process of macropore-facilitated preferential flow, transport through cracks within a soil matrix, has been recognized to increase radionuclide mobility (Bundt, 2000). The aim of this study is to clarify the influence of macropore structures (orientation and geometry) on the transport of ^{99}Tc and ^{237}Np in unsaturated sand and sandy clay loam (SCL) soils.

Unsaturated column flow experiments were completed with Br (tracer), ^{99}Tc, and ^{237}Np on homogeneous and macroporous soil columns. CT scans of soil columns were acquired to generate 2D and 3D imaging of macropore networks. Retardation factors for Tc^{99} breakthrough were 1.30 in homogeneous SCL and ranged from 1.28 to 1.41 in macroporous SCL, indicating that macropore-facilitated bypass flow is limited in unsaturated conditions. However, ^{99}Tc exhibited earlier initial arrival (IBV) and longer attenuation in macroporous SCL soils. Increasing dispersivity estimates, determined by fitting the two-region nonequilibrium convection dispersion equation (MIM), well describe the anomalous breakthrough trends observed in macroporous SCL soils. From these findings, we conclude that macropore structures oriented transverse to unsaturated flow act as capillary barriers (resulting in longer radionuclide attenuation). If vertically oriented, macropore structures act as capillary boundaries that isolate matrix flow to a fraction of the pore network (increasing the average porewater velocity and IBV).

ACKNOWLEDGMENTS

KEYWORDS

Preferential flow, vadose zone, unsaturated flow, macropore flow, macropore network, capillary exclusion, radionuclide transport, technetium-99, Tc-99, neptunium-237, Np-237, bromine, bromide, Br, Savannah River Site, SRS, non-equilibrium transport, residence time distribution analysis, RTD, temporal moments analysis, spatial moments analysis, two-region non-equilibrium transport model, mobile-immobile model, MIM, mobile-fluid region, immobile-fluid region, convection-dispersion equation, CDE, spent nuclear fuel storage, SNF, dispersivity, mobile water fraction, mass transfer coefficient, CXTFIT, pore volume, sandy clay loam, sand, soil, sorption, partitioning coefficient, K_d, column flow experiment, column tracer test, mean arrival time, MAT, mean travel time, MTT mean arrival pore volume, MAPV, mean travel pore volume, MTPV, retardation factor, CT scanner, MILabs, U-CT scanner, soil structures, 3D macropore network reconstruction, heterogeneity, and effluent.

TABLE OF CONTENTS

LIST OF TABLES

LIST OF FIGURES

CHAPTER 1:   INTRODUCTION

1.1   Background

The presence of radionuclides in the environment poses long-term impacts on human health and ecosystems. The proliferation of these contaminants across the United States rose with the development of nuclear weapons and nuclear energy in the 1950s (DOE/NE-0088). During this time period, limited regulations enabled the disposal of radioactive byproducts and waste in unlined pits and settling basins. Since then, the United States has produced approximately 90,000 metric tons of spent nuclear fuel (SNF) (Office of Nuclear Energy, 2022). Permanent storage plans of SNF within the vadose zone have been proposed at Yucca Mountain in Nevada (Eckhardt et al., 2000). High-level radioactive liquid waste is also generated as a byproduct of processing nuclear materials. DOE generated high-level waste and Cold War era legacy waste is stored at DOE operated nuclear industrial complexes such as the Savannah River Site (SRS) in Aiken, SC.

The migration of radionuclides in the environment is dependent on physical, geochemical, and biological processes unique to the environment affected (Seaman et al., 2012). A critical component in assessment and remediation efforts is the development of transport models that incorporate the processes that govern radionuclide mobility. To build and validate site-specific radionuclide transport models, interdisciplinary research efforts must be applied.

In recent years, research has been conducted to define the governing transport processes, generate comprehensive transport models, and accurately estimate and scale radionuclide model parameters (Massabó, 2011; Brouyère, 2006; Dagan and Cvetkovic, 1993;

Ababou, 1991; Van Genuchten & Wagenet, 1989). Vadose zone transport is made complex by preferential flow, variable spatiotemporal redox conditions, and chemical non-equilibrium adsorption. Furthermore, predictive modeling of radionuclide transport at the field-scale has been challenged by the issue of scale-dependent parameterization. Thus, the assessment of radionuclide vadose transport requires multi-scale, site-specific studies coupled with reactive and numerical transport models (Moradi, 2020).

1.2   Significance: The Savannah River Site

The Savannah River Site (SRS) is a 300,000 square mile nuclear reserve located in Aiken, South Carolina (DOE/NE-0088). SRS is home to 51 underground radioactive waste storage tanks (Area's F and H). Four of these tanks have been permanently closed and 20 tanks are lacking secondary containment, violating EPA regulations. No leaks are currently reported from these tanks; however, 12 of the 20 tanks in violation have a history of leaking (U.S. NRC, 2021). Recent DOE documents report that SRS presently stores 1.4×10^8 L (36 Mgal) of liquid radioactive waste, amounting to ~ 400 MCi of radioactivity (Wilmarth, 2011).

Historically, nuclear reactors at this site produced weapons-grade tritium and plutonium. The fabrication of these materials produced uranium-bearing waste that was disposed of on-site in settling basins and unlined pits. Recent studies have estimated that 83% of the uranium released into the environment is now sequestered in a wetland onsite (Kaplan et al., 2020). Kaplan et al. (2020) found that sorption of uranium to wetland soils at SRS effectively immobilized the leached uranium. However, other long-lived actinides with variable sorption characteristics may not have the same fate if released into the environment.

During nuclear fuel reprocessing, waste is generated with significant concentrations of ^{99}Tc, and ^{237}Np (Hu, 2010). With half-lives of 2.13 x 10^5 and 2.14 x 10^6 years respectively, and high mobility in oxidizing conditions, these radionuclides pose a significant risk for human exposure if leached into surface or groundwater systems. To accurately assess and predict the fate of ^{99}Tc and ^{237}Np at SRS, site-specific transport models coupling hydrologic and geochemical processes must be expanded upon.

1.3   Preferential Flow

Characterizing flow and transport in the vadose zone has been a challenging yet promising field of research in recent years (Zhang, 2018). As many radionuclide contaminant sources are located in the vadose zone, it is critical to further our understanding of transport in this subsurface region. Flow and transport in the vadose zone is, in part, complicated by the phenomena of preferential flow. The physical process of preferential flow was described by Hendrickx and Flury (2001) as the channeling of infiltrating water and solutes through a small fraction of a pore-network. The variable mechanisms of this phenomenon are distinguished by three unique types of preferential flow: macropore flow, fingered flow, and funnel flow (Stumpp, 2022). During funnel flow, the preferential flow of water is dependent on localized heterogeneities. For example, a clay lens within a sandy loam matrix will redirect the flow of infiltrating water to a preferential flow path. Fingered flow occurs in unstructured course-grained soils and is described as an unstable wetting front (Zhang, 2018). This unstable wetting front is a product of opposing capillary and gravitational forces that generate fingered flow paths. Lastly, macropore flow refers to the preferential flow of water through soils that contains pore-scale heterogeneities, i.e., fractures (Jarvis, 2016). These macropore structures

can form from both biological and physical processes. The wet-dry cycling of clay soils has been shown to generate macro-pore structures that enable preferential flow (Schlüter 2016; Pires 2020; Al-Mamun 2022), and coarse root systems have also been found to increase soil macro-porosity (Bodner et al., 2014).

Noted by Mamun (2022), the orientation and geometry of macropores largely impacts the advective, diffusive and preferential transport processes that occur during infiltration events. Mamun states that vertical macropores enable matrix bypassing flow and transport during infiltration. Transport across horizontal macropores is mediated by the formation of droplets within the macropore or through capillary bridges. However, they can act as capillary barriers to evaporative upward transport, decreasing the net downward flux (Mamun 2020).

As hydrologic conditions transition from equilibrium flow to macropore flow, spatial variations of both flow velocities and solute concentrations are observed within the pore-network. Radionuclides have an affinity to sorb to soils with high iron-hydroxide (FeOH) compositions (Kaplan et al., 2018). Under the geochemical conditions at the SRS, ^{99}Tc and [237]Np show weak sorption to soil minerals and are generally mobile in the subsurface (Montgomery, 2017; Powell, 2018; Peruski, 2018). Non-uniform fluid and solute distributions in soils at the macro-scale will reduce the contact between solutes and potential FeOH sorption sites. Effectively, this process can limit a soil's ability to retard radionuclides in transport. The extent to which preferential flow processes impact the adsorption of mobile radionuclides such as ^{99}Tc and [237]Np is currently not well defined. Moreover, adsorption is just one process that governs the retardation of radionuclides in transport. Advection, and chemical precipitation are all other

processes that influence the transport of radionuclides and can be impacted by preferential flow (Luo et al., 2000).

1.4   Soil Properties and Geochemistry

To properly evaluate the behavior of ^{99}Tc and ^{237}Np in the environment, the soil properties of the region studied must be determined. In this study, experiments will be designed to replicate vadose zone conditions at the SRS. The soil classification, pH, redox potential, iron content, and natural organic matter (NOM) content are all critical parameters to define at this site. Sand and sandy clay loam (SCL) soil was collected from borrow pits located on-site at SRS. The region is rich in deposits of SCL (66% sand, 14% silt, 20% clay) and acidic with groundwater pH measurements ranging from 3.2 to 6.8 (Otosaka, 2011). Assuming this pH range and aerobic conditions, technetium will dominantly speciate in the heptavalent state as pertechnetate (TcO4 -), a water-soluble oxyanion of technetium, and neptunium will speciate in the pentavalent oxidation state. The mobility of these species in soil is impacted by the process of adsorption. Iron-bearing surface minerals act as sorption sites in soils; therefore, quantifying the extractable iron in sediments can enable the prediction of a radionuclide's relative mobility at a site (Kaplan et al., 2018). Iron concentrations, extracted via citrate buffered dithionite (CBD), in sandy clay loam (SCL) soils from SRS were found to have a concentration of 6.01 ± 0.68 mg/g (Table 1.1) In SRS SCL soils, sorption of ^{237}Np is relatively stronger than ^{99}Tc. Partitioning coefficients (K_d) values estimated for ^{99}Tc and ^{237}Np in this same soil were -0.2 and 5.5 cm^3 g^{-1} (Montgomery, 2018).

Table 1.1   Soil Properties and Characteristics

Parameter	Unit	Value
Soil classification	-	Sandy clay loam (SCL)
Sand / Silt / Clay	%	66 / 14 / 20
Soil porosity, Θ	-	0.35
Hydraulic conductivity, k	m s^{-1}	6.31E-6
Point of zero charge, pzc	-	4.9 [a]
NOM content	%	0.9 [a]
Iron content (CBD-extractable)	mg g^{-1}	6.01 ± 0.68 [a]
SRS Groundwater pH	-	3.2 – 6.8 [b]

[a] Montgomery, 2017

[b] Otosaka, 2011

CHAPTER 2:   OBJECTIVES AND HYPOTHESES

2.1   Objectives

The objective of this study is to characterize the impacts of macropore structures on ^{99}Tc and ^{237}Np transport in unsaturated soils from SRS. The experimental design focuses on the flow and transport processes: macropore flow, matrix diffusion, and capillary exclusion. The aim of this study is to observe macropore generation in soils during wetting-drying events, identify dominant transport processes in macroporous sand and SCL, and clarify the roles macropore orientation and geometry play in radionuclide migration.

This experimental study, broken up into four prominent tasks in Table 2.1, is designed evaluate the current transport model established for ^{99}Tc and ^{237}Np at SRS, and assess the effects of macroporosity on physical and chemical transport processes. These tasks produce: 1) baseline transport datasets for Br, ^{99}Tc, and ^{237}Np in SRS soils with homogenous soil structures, 2) provide qualitative imaging of macropore structures generated from a wetting and drying event of sandy clay loam soils, 3) quantitatively evaluate ^{99}Tc and ^{237}Np mobility under heterogeneous flow conditions, and 4) estimate site-specific modeling parameters. By executing these tasks, one can make conclusions applying to the nature of radionuclide transport at SRS, and how these transport processes are impacted by macropore-facilitated preferential flow.

Table 2.2   Experimental Tasks and Objectives

Tasks	Objectives
Task 1 Execute a preliminary lab-scale column flow test under homogenous pore-structure conditions with sand and a sandy clay loam from SRS	Evaluate the experimental design and determine baseline elution curves for Br, ^{99}Tc, and ^{237}Np
Task 2 Acquire pore-structure imagery of lab-scale soil columns pre- and post-wet-dry event	Assess the impacts of environmental wetting and drying events on macropore structures in unvegetated sands and sandy clay loam soils
Task 3 Execute lab-scale column flow experiments on unvegetated soil columns that have been exposed to wet-drying conditions	Determine the influence that macropore structures have on ^{99}Tc, and ^{237}Np mobility in unvegetated sands and sandy clay loam soils
Task 4 Simulate column flow experiments using non-equilibrium convection-dispersion Eqn. (MIM model) and statistically fit to experimental results	Establish site-specific modeling parameters (i.e., dispersivity, mobile water fraction, and mass transfer coefficient) and quantify the impact of macropore flow on these parameters

2.2   Hypotheses

With the objectives outlined in Table 2.1, this study will expand upon environmental transport models previously done for the Radionuclide Field Lysimeter Experiments (RadFLEx) at SRS (Kaplan et al., 2004; Demirkanli et at., 2007; Demirkanli et at., 2008; Demirkanli et at., 2009; Molz et al., 2015). It is hypothesized the presence of macropore networks in soils will decrease the number of active flow paths within a pore network, effectively decreasing the pore volume used by mobile fluid and increasing local flow velocity variations. Flow regimes with a decreased effective pore volume and wider distribution of flow velocities will show both earlier arrival and longer attenuation of ^{99}Tc and ^{237}Np. This is simplified by stating the presence macropores networks will separate the soil matrix into mobile and immobile fluid regions, which correspondingly enhances and limits advective (physical) transport. It is also

hypothesized that increases in solute flux through a smaller (mobile) fraction of the pore matrix will decrease chemical adsorption of ^{99}Tc and ^{237}Np by limiting the number of interactions between radionuclides and sorption sites. These hypotheses will be evaluated by interpreting mean arrival estimates (moments analysis) and parameter fitting of column breakthrough with the 1D mobile-immobile (MIM) transport model.

CHAPTER 3:   METHODS

3.1   Experimental Design and Setup

In this study, unsaturated flow column experiments were executed at the lab scale to progress our understanding of preferential flow and its impacts on ^{99}Tc and ^{237}Np transport in sandy clay loam soils. To describe simply, a spike solution containing a contaminant and a non-reactive tracer is first added to the packed sediment column. While maintaining a constant flow rate, the column is then flushed with a wash solution (DI) for a given number of pore volumes. Effluent samples are collected at time intervals throughout this process and analyzed to produce breakthrough curves. In our application, these laboratory experiments were designed to replicate the environmental conditions of the vadose zone at SRS while evaluating contaminant mobility in a laboratory environment.

Column Preparation

Unsaturated column flow tests were completed using polyethylene columns (column I.D. = 3.75 cm, h = 18 cm) packed with either a sandy clay loam or sand (Figure 1). To ensure sediments were initially packed homogenously, sediment was added in two-centimeter increments. In between each layered addition, the column was tapped on a hard surface to allow for sediment to settle. Additionally, the top surface of each layer was scarified with a scoopula to ensure any overlying layers were coupled and well mixed. Once packed, select columns were exposed to wetting and drying cycles to replicate the conditions that sediments endure in the vadose zone. This process consisted of fully saturating each column with

Figure 1   Sandy clay loam (SCL) and sand packed columns (d = ~ 14 cm) used in column flow experiments. Columns are pictured prior to exposure to wet-drying event.

deionized water, allowing them to fully drain, and then dry at room temperature for over two months. With the exception to sand and sandy clay loam control columns (*SCL_H_1* and *S_H_1*), all columns were exposed to one wet-drying event (Table 3.1). Pore volume estimates of each column were determined by saturating each column and comparing the dry and saturated weights. The sand and sandy clay loam control columns (*SCL_H_1* and *S_H_1*) were saturated 48 hours prior to experimental testing to determine their pore volume and initially wet the soils. To minimize the trapping of air in pores during this process, all columns were filled from the bottom up via capillary tubing and a peristaltic pump (Figure 1).

Table 3.3   Outline: Unsaturated Column Flow Experiments

Exp. #	Column ID	Soil Type	Environmental Conditions	Initial Water Saturation
H_1	SCL_H_1	Sandy clay loam	Control	Pre-saturated
	S_H_1	Sand		
M_1	SCL_M_1	Sandy clay loam	Wet-dry cycled	Dry
	S_M_1	Sand		
M_2	SCL_M_2	Sandy clay loam	Wet-dry cycled	Pre-saturated
	S_M_2	Sand		
M_3	SCL_M_3	Sandy clay loam	Wet-dry cycled	Pre-saturated
	S_M_3	Sand		

Unsaturated Column Flow Experiments

The column flow experiments applied in this study maintained unsaturated conditions by adding the influent solution at a constant volumetric flow rate of ~ 0.1 mL/min. Estimates of the soils hydraulic conductivity are 6.31×10^{-1} m s^{-1} and column's inner diameter was 3.75 cm (cross-sectional area = 1.1×10^{-3} m^2). Using this configuration and flow rate, darcy flux through the column is estimated to be 4.1×10^{-6} m s^{-1}. As the flux remains smaller than the soils hydraulic conductivity, unsaturated conditions theoretically will be maintained.

During experimentation, a peristaltic pump connected to capillary tubing was used to drip the influent solution onto the top-soil surface at a constant rate (Figure 2). A spike solution containing Br, ^{99}Tc, and ^{237}Np was prepared in 2% HNO$_3$. Each experiment was initiated by the addition of the spike solution. The spike solution volume added varied between experiments varied from of 0.69 to 1.0 pore volumes. Once the spike solution was added, the influent solution was switched to a bottle of deionized (DI) water which was used to flush the column
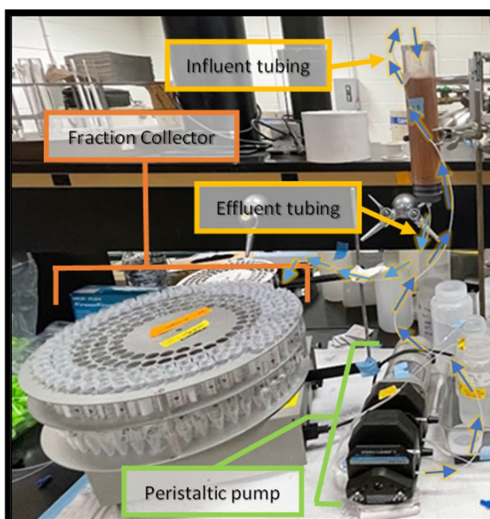
Figure 3   Laboratory setup for unsaturated column flow experiments. Label experimental components include influent line, effluent line, fraction collector, and peristaltic pump.
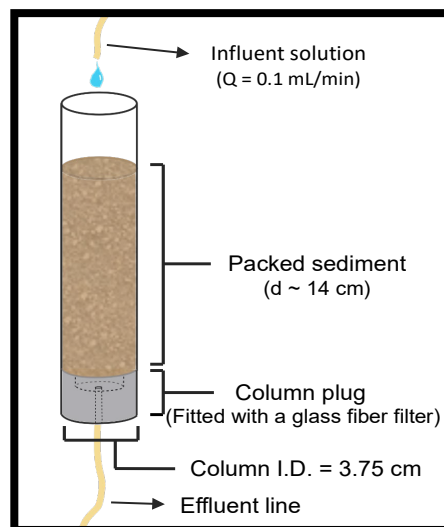
Figure 2   Schematic of unsaturated column flow experiment

for a minimum of 5.0 pore volumes following the spike solution. For the duration of the experiment, the effluent solution gravity drained through a glass fiber filter fitted at the base of the column and was collected with 15 ml centrifuge tubes using and Eldex fraction collector (Figure 2) In each column flow experiment, samples were collected every 30 minutes for the first 80 samples and at one-hour increments for the final 30 samples. With an influent flow rate of 0.1 mL/min, each experiment ran for just over three days.

Peristaltic Pump Calibration

The peristaltic pump, responsible for adding the spike and DI water influent solutions in each column experiment, was calibrated to accurately set and maintain a constant flow rate. The *Masterflex L/S Easy-Load II* peristaltic pump, equipped with dual pump heads and a 1-100 RPM motor, was used for all column flow experiments. For this model, the pump head rotation speed is controlled by a unitless manual dial, also known as a potentiometer. To calibrate this dial to pump at a flow rate of 0.1 mL min^{-1}, the pump tubing diameter and length were first configured identically when used for experiments. The pump was then turned on at an arbitrary pump speed, and a volume of pumped water was collected and weighed at 10 min intervals. The dial position of the potentiometer was marked to establish a reference point associated with the calculated flow rate for each collection. The dial was then lowered, and this process was repeated until the flow rate of 0.1 mL min^{-1} was bounded on upper and lower ends within a tolerance of 0.02 mL min^{-1}. The upper and lower bounds were marked on the potentiometer to reproducibly set the desired flow rate.

3.2   Effluent and Sediment Analysis

Core Sectioning

Within 24 hours after each unsaturated flow experiment, sediment columns were reweighed, scanned via x-ray computed tomography, and sectioned into 1 cm increments. Each sediment column was sectioned from bottom to top with a sediment core extruder. The column plug from the base of the column was first removed to allow for sediment to be extruded from the outlet. A plunger cap was then placed on the top of the sediment core, and the column was inverted. With the column orientation reversed in the press, the bottom sediment was extruded first. All columns were sectioned from bottom to top because the highest sorbed concentrations were estimated to remain in the top 5 cm of the column. Extruding the upper 5 cm last minimized any smearing and cross-contamination of sediment sections in the column.

When mounted in the press, a threaded extrusion rod was tightened with a socket wrench to extrude sediment in controlled increments (Figure 4). Each section was sliced in 1 cm increments, transferred into aluminum dishes, and weighed. Post-sectioning, all sediment samples were immediately placed in an oven and dried at 48ºC for 72 hours. Pre- and post-drying sediment weights were recorded and used to calculate water content profiles for each column.

Figure 4   Sediment core extruder used to section sediment columns into ~ 1 cm intervals

Sediment Digestions

Dried core sections were digested to quantify the sorbed mass fraction of ^{99}Tc and ^{237}Np at depth. Sediments were digested with a 4:1 nitric acid to sediment ratio (by weight). First, approximately 20 g (~ 12.5 mL) of sediment was transferred from aluminum dishes into 50 mL centrifuge tubes, suspended in 30 mL of ~ 5.3 M HNO_3, and shaken on a shaker table for 72 hours. The sample digestions were later centrifuged at 4500 rpm for one hour. The supernatant was then decanted into new centrifuge tubes. The efficiency of each digestion was not directly measured with an internal standard; however, each experimental dataset was holistically validated with mass balance calculations.

Analytical Instrumentation

Elemental analysis of effluent samples and sediment digestions was primarily completed via inductively coupled plasma–mass spectrometry (ICP-MS). All ICP-MS analysis was performed with a Thermo Scientific iCAP™ RQ analyzer equipped with a quadrupole mass spectrometer. In preparation for elemental analysis of effluent samples, 0.5 mL subsamples were diluted by a factor of four with ~ 0.5 M HNO_3. Similarly, sediment digestions were diluted by a factor of 10 to reduce matrix interferences. During ICP-MS analysis, an internal standard solution containing ~ 10 ppb ^{6}Li, Sc, Bi, Ga, In, Tb, and Y was run alongside standards and samples to correct for variations in sample uptake, detector response, and or matrix interference. Once quantified, datasets were used to generate Br, ^{99}Tc, and ^{237}Np breakthrough curves and sorbed ^{99}Tc and ^{237}Np profiles. These datasets were collectively used to complete a mass balance for each experiment. Liquid scintillation counting (LSC) was intermittently used across this study to verify ^{99}Tc and ^{237}Np spike and effluent concentrations determined via ICP-MS.

Pore-scale Imaging

Pore-scale imaging of soil columns was achieved via X-ray computed tomography (CT) scanning (MILabs U-CT scanner)(Figure 5). Utilizing the same concepts as medical CT scanners, X-rays are emitted at an object and detected by a digital detector positioned opposite of the beam source. The attenuation, or intensity reduction, of transmitted X-rays, increases with material density. From these scans, cross-sectional images are computed so that pixel intensities are dependent on localized density contrasts across the object. Image processing software can then be used to stack the acquired slices into a reconstructed volume.

Figure 5   MILabs U-CT scanner equipped with a vertical bore used to investigate soil structures present in SCL and sand packed columns

Throughout a sediment column, density contrasts exist between soil, pore-water, and air interfaces within the micro- and macro-pore networks. The effective application of computed tomography to identify macropore structures is dependent on the instrument's scanning resolution. The MILabs U-CT scanner has a minimum voxel resolution of 30 μm^3 (MILabs 2022). CT scans of soil columns were image processed with a voxel resolution of 60 μm^3 to capture alterations of the pore structure at this scale. Equipped with a vertical bore, the MILabs U-CT scanned sediment columns while positioned in an upright orientation.

3.3 Data Analysis

Overview: Moments Analysis

Lab-scale column flow experiments completed in this study were developed to characterize the mobility of ^{99}Tc and ^{237}Np in homogenous and heterogeneous pore networks. Moment's analysis was applied to normalize varying factors across column flow experiments, produce mass and volume balances for effluent data, and evaluate solute breakthrough curves and sorbed solute distributions. When applied to outflow data from column flow experiments, characteristic temporal moments indicate the total mass eluted, mean arrival time, the extent of spreading, and skewness. Spatial moments were used to quantify analogous parameters that are determined from sediment concentration profiles.

The zeroeth, first, second, and third moment from Br, ^{99}Tc, and ^{237}Np breakthrough curves and ^{237}Np sorption profiles following general equations 1 and 2 (Shook, 2005). Temporally, nth moments correspondingly evaluate the total mass eluted, mean arrival time, variance, and skewness. Spatially, they represent the total adsorbed mass, mean travel distance, variance (plume spread), and skewness.

$$\mu_n = \int_0^{t_f} C t^n \, \mathrm{d}t = \sum C \, t^n \Delta t \qquad\qquad \text{Eqn. 1}$$

$$\mu_n = \int_0^{t_f} C z^n \, \mathrm{d}z = \sum C \, z^n \Delta z \qquad\qquad \text{Eqn. 2}$$

Equation 1 states that the nth moment (μ_n) is generally determined by integrating the product of concentration and time to the nth power with respect to time. Spatial moments analysis will follow formulations identical to the temporal moments analysis described in the following sections (*Ch. 3, sect. 3.3 − 5.5*) but with respect to distance (*z*) where z is equal to sediment depth (*Eqn. 2*).

Given that breakthrough curve datasets are comprised of a finite set of time-series

effluent concentrations, numerical integration was used to approximate these integrals. The

trapezoid method, equation 3, was used to evaluate n^{th} moments for experimental data. This

integration method, approximating the area under a curve from the sum of subdivided

trapezoids, was selected because of its ease of application and increased accuracy over

numerical integration methods such as the midpoint method.

$$\int_a^b f(t)\,dt \approx \frac{\Delta t}{2}[f(t_0) + 2f(t_1) \ldots 2f(t_{n-1}) + f(t_n)] \qquad \text{Eqn. 3}$$

Applications: Zeroeth Temporal Moment

The zeroeth moment, (μ_0), interpreted as the total mass eluted out of the column in

units of length, was first calculated to normalize subsequent moment calculations and to

generate a mass balance for eluted solutes from the spike solution. Traditional effluent mass

balance calculations are made by comparing the ratio of the total mass eluted (M_{out}) over the

total mass input (M_{in}) into the system. M_{in} is typically calculated as the spike concentration (C_0)

multiplied by the volume added and M_{out} is equivalent to the integral of eluted concentration

multiplied by the volumetric flow rate with respect to time (Eqn. 4). Alternative to this

approach, the zeroeth moment (Eqn. 5 & 6) in which *C(t)* was substituted with *C/C₀*, was applied

to determine M_{out}. This formulation operates under the assumption that the volumetric flow

rate throughout the experiment is constant. This calculation measures the mass input quantity

in units of time instead of mass. Assuming a constant injection flowrate, the mass input

measured in time (M_{t_in}) is equal to the spike pulse time (t_0) (Eqn. 5). For mass balance

calculations, the total mass output in units of time is symbolized by M_{t_out} but is noted as μ_0^* for

subsequent moment calculations. The moment follows equation 6, where effluent

concentrations normalized by the spike concentration (C/C_0) are integrated over the

breakthrough dataset with respect to time (Eqn. 4). For simplification, normalized

concentrations are noted as C^* (Eqn. 7).

$$M_{out} = \int_0^\infty QC(t)\,dt \quad [M] \qquad\qquad \text{Eqn. 4}$$

$$\frac{\bar{Q}_{out}}{\bar{Q}_{in}} = 1 \quad \rightarrow \quad M_{t\_out} = \mu_0^* = \int_0^\infty \frac{Q_{out}(t)}{Q_{in}(t)}\frac{C(t)}{C_0}\,dt \quad [T] \qquad\qquad \text{Eqn. 5}$$

$$\mu_0^* = \int_0^\infty C^*(t)\,dt \quad [T] \qquad\qquad \text{Eqn. 6}$$

$$C^*(t) = \frac{C(t)}{C_0} \quad [-] \qquad\qquad \text{Eqn. 7}$$

Effluent mass balances were completed for Br ^{99}Tc and [237]Np across all experiments by

integrating normalized concentrations over time. Normalized concentration (C^*), ranging from 0

to 1, is dimensionless. This means that when integrated over time, the total mass out (μ_0^*) is

approximated in units of time and corresponds to the pulse duration of the spike. Thus, μ_0^*

increases to t_0 as the effluent tracer or solute recovery approaches 1. Times at which the pulse

started and stopped were recorded with a stopwatch for each experiment. However,

considering its role in accurately evaluating the percent recovery, t_0 was verified by initial and

final volumetric measurements of the spike solution. By recording the change in spike volume

after each experiment and calculating the average volumetric injection flow rate some fraction

collected samples, the noted t_0 measurements were verified. In summation, the effluent

recovery of each solute was calculated from the ratio of mass output (M_{t_out}), determined by

the zeroeth moment, divided by mass input (M_{t_in}), determined volumetrically (Eqn. 8).

$$\% \, Recovery = \frac{M_{t\_out}}{M_{t\_in}} = \frac{\mu_0^*}{t_0} \qquad\qquad \text{Eqn. 8}$$

Applications: First Temporal Moment

The absolute first moment (μ_1^*), found from integrating the product of C/C_0 and time with respect to time, characterizes the absolute mean arrival time of the solute (Eqn. 11). With units of time squared, the absolute mean arrival time must be normalized by a characteristic time unique to the dataset to acquire a first moment that is meaningful in this analysis. The zeroeth moment, representative of the total mass injected in units of time (Eqn. 6), was used to normalize the first moment (Eqn. 10). The normalized first moment ($\hat{\mu}_1^*$) represents the center of mass of the breakthrough curve or the average travel time of the plume. For breakthrough curves with ~ 100% recovery, the recovery is 50% at the mean arrival time.

$$\mu_1^* = \int_0^\infty C^*(t)t\, dt \quad [T^2] \qquad\qquad \text{Eqn. 9}$$

$$normalized\ \mu_1^* = \hat{\mu}_1^* = \frac{\int_0^\infty C^*(t)t\, dt}{\int_0^\infty C^*(t)dt} = \frac{M_1}{M_0} \quad [T] \qquad\qquad \text{Eqn. 10}$$

The normalized first moment, also known as the mean arrival time (MAT), was used to determine the mean travel time (MTT). MTT, equivalent to the retardation factor (R) in units of pore volumes, was calculated from the MAT minus the average pulse time of the spike solution (Eqn. 11). MTT values were converted from units of time to units of pore volumes injected by multiplying MTT by the average volumetric flow rate and dividing by the pore volume (V_p) (Eqn. 12). C/C_0 should reach a value of 0.5 at the mean travel pore volume (MAPV). The partitioning coefficient (K_d) was calculated for each analyte across all planned experiments (Eqn. 13). This value describes the sorption affinity of an analyte to the soil. The partitioning coefficient can be determined by dividing the retardation factor minus one ($R - 1$) by the dry bulk density of the soil (ρb) and multiplying that by the porosity of the soil (Θ). This calculation assumes that retardation in experiments is 100% dependent on equilibrium sorption which does not align

with this study's conceptual model; therefore, the contaminant mobility will be evaluated only by experimentally derive R.

$$MTT = \hat{\mu}_1^* - 0.5 * t_0 \qquad \text{Eqn. 11}$$

$$R = \frac{MTT \cdot \bar{Q}}{V_p} \qquad \text{Eqn. 12}$$

$$K_d = \left(\frac{R-1}{\rho b}\right)\theta \qquad \text{Eqn. 13}$$

Lastly, this formulation allows for the volume fraction of the soil column to be determined. Considering the presence of macropores in a soil can separate pore matrix into mobile and immobile regions, solving for this value is of interest. The volume fraction [L^3], is used as a direct comparison to pore volume measurements completed experimentally (Eqn. 14).

$$V = \frac{\bar{Q}}{\hat{\mu}_1^*} \quad [L^3] \qquad \text{Eqn. 14}$$

Applications: Higher Order Temporal Moments

The second moment ($\hat{\sigma}$), also known as the variance, describes the spread of the plume about its mean arrival ($\hat{\mu}_1^*$) following equation 15. As the variance value increases, the distribution of concentration away from the mean or spreading increases and acts as an indicator of dispersive transport processes.

$$\hat{\sigma} = \frac{\sigma}{\mu_0^*} = \frac{\int_0^\infty (t - \hat{\mu}_1^*)^2 C^*(t)dt}{\mu_0^*} \qquad \text{Eqn. 15}$$

The third moment (*SK*) signifies the degree of asymmetry for a breakthrough curve. This quality is termed as skewness; whereas *SK* decreases towards zero, the shape of the peak approaches a gaussian distribution. For column flow tests, transport processes such as matrix diffusion and non-equilibrium flow conditions can cause an elution curve to show a longer

extended tail as the last fractions of the tracer or spike elute. The skewness value enables the

degree of tailing to be quantified (Eqn. 16).

$$\text{SK} = \hat{s}^3 = \frac{S^3}{\mu_0^*} = \frac{\frac{1}{\hat{\sigma}^{3/2}}\int (t-\hat{\mu}_1^*)^3 C^*(t)\,dt}{\mu_0^*} \qquad \text{Eqn. 16}$$

Temporal Moments Analysis with Variable Flow Rate

In this study's experimental setup, constant volumetric flow rates were maintained

using peristaltic pumps. Even after proper calibration and maintenance, these pumps can

introduce unwanted flow rate variations. A moments analysis formulated to account for

changes in flow rate was applied to determine if flow rate observations produced deviating

results. Using a similar formulation seen in equations 4 through 16, the general formula follows

equation 17, where Q is the volumetric flow rate, C is concentration, and t^n is time to the nth

power corresponding to the order of the moment calculated. The zeroeth moment, assuming

variable flow rates are observed, is described in equation 4. The residence time distribution

curve, calculated by the function $E(t)$, can be defined by *equation 18,* where it represents the

fraction of the tracer passing through the outlet at a given time. This function is used to solve

for the first temporal moment (Eqn. 18 & 19) and normalizes the data by the total mass

recovered, analogous to the purpose of equation 11. Retardation factors were recalculated

using this formulation and compared with values generated to evaluate error introduced by

volumetric flow rate variations.

$$\mu_n = \int_0^\infty Q\,C\,t^n\,dt = \sum Q\,C\,t^n \Delta t \qquad \text{Eqn. 17}$$

$$E(t) = \frac{C_{out}(t)Q}{\int_0^\infty C_{out}(t)Q\,dt} \quad [T^{-1}] \qquad \text{Eqn. 18}$$

$$\hat{\mu}_1 = \int_0^\infty tE(t)\,dt \quad [T] \qquad \text{Eqn. 19}$$

3.4   Modeling

Two-region Nonequilibrium Convection-Dispersion Model (MIM)

Many deterministic and stochastic modeling approaches have been successfully applied to simulate solute transport in heterogeneous soils (Dagan and Cvetkovic, 1993; Kabala, 1991; Ababou, 1991). Traditionally, the flow regime of unsaturated and homogenous systems has been well described by Richard's equation and chemical transport by the convection-dispersion equation (CDE) (Richards, 1931; Massabó, 2011). However, flow and transport in heterogeneous soils presents anomalous trends that these approaches have failed to describe. As stated in chapter one, macropore structures in soils can produce preferential flow paths for infiltrating water, effectively bypassing the micropore matrix; however, studies suggest this activity is dependent on saturation and macropore orientation (Brouyère, 2006; Mamun, 2022). This anomalous behavior is indicative of nonequilibrium flow and transport. Van Genuchten and Wagenet (1989) derived an altered CDE that is able to simulate anomalous behavior better than the traditional CDE (Padilla, 1999). The two-region nonequilibrium CDE (MIM) assumes that only a fraction of the liquid phase is mobile in heterogeneous soils. By separating the model domain into mobile and immobile regions, solute transport can be cumulatively described by convective-dispersive (matrix flow) and the rate of exchange between mobile and immobile regions. With a dual porosity-like formulation, the MIM model has been proven to describe equilibrium and nonequilibrium solute transport at field and lab scales (Padilla et al., 1999; Brouyère, 2006; Blackmore et al., 2014).

In the dimensionless form (Eqn. 4 & 5), MIM can be applied to describe physical or chemical nonequilibrium transport. Applications for chemical nonequilibrium adsorption utilize

the "two-site" formulation where, as physical nonequilibrium is described by the two-region

formulation (van Genuchten and Wagenet, 1989; Nkedi-Kizza, 1984).

$$\beta R \frac{\partial C_1}{\partial T} = \frac{1}{P} \frac{\partial^2 C_1}{\partial Z^2} - \frac{\partial C_1}{\partial Z} - \omega(C_1 - C_2) - \mu_1 C_1 + \gamma(z) \qquad \text{Eqn. 20}$$

$$(1 - \beta)R \frac{\partial C_2}{\partial T} = \omega(C_1 - C_2) - \mu_2 C_2 + \gamma(z) \qquad \text{Eqn. 21}$$

The dimensionless terms are presented as, β, R, C, T, P, Z, ω, μ, and γ. Utilizing the two-

region model, subscripts 1 and 2 are indicative of equilibrium (flow) and non-equilibrium liquid

regions. β represents the fraction of mobile water in the continuum. By setting $\beta = 1$, solute

transport is defined only by equilibrium processes where Eqn. 5 is voided, and effectively, the

MIM model is restored to the traditional CDE. The peclet number, P, is defined as the ratio

between the mobile liquid velocity (v_m) multiplied by a characteristic length (L = column height)

and the dispersion coefficient (D_m) (Eqn. 7). The peclet number is interpreted as an indicator of

whether advective ($P \gg 1$) or dispersive ($P \ll 1$) transport processes are dominant.

$$P = \frac{v_m L}{D_m} = \frac{vL}{D} \qquad \text{Eqn. 22}$$

The mass transfer coefficient, ω, governs the rate of exchange between mobile and

immobile regions. This term is translated to its dimensional form from the relationship seen in

Eqn. 8, where alpha, α, is the dimensional mass transfer coefficient.

$$\omega = \frac{\alpha L}{\theta v} \qquad \text{Eqn. 23}$$

Where μ, is the degradation coefficient, and γ is the zeroth order production term for

mobile and mobile phases. Within the experimental scope of this study, it was assumed that

both degradation and production terms are negligible. Dimensionless time (T), concentration

(C), and distance (Z) are respectively defined in equations 24, 25, & 26.

$$T = \frac{vt}{L} \quad \text{(Eqn. 24)} \qquad C = \frac{C_m}{C_0} \quad \text{(Eqn. 25)} \qquad Z = \frac{x}{L} \quad \text{(Eqn. 26)}$$

As described by Toride (1993), the two-region nonequilibrium CDE is written in its

dimensional form in Eqn. 27 & 28.

$$(\theta_m + f \rho_b \, k_d) \, \frac{\partial C_m}{\partial t}$$

$$= \theta_m \frac{\partial}{\partial x} \left[D_m(x) \frac{\partial C_m}{\partial x} \right] - v_m \theta_m \frac{\partial C_m}{\partial x} - \alpha(C_m - C_{im})$$

$$- \left(\theta_m \mu_{im} + f \rho_b k_d \mu_{s,m} \right) C_m$$

Eqn. 27

$$[\theta_{im} + (1 - f) \, \rho_b \, k_d] \frac{\partial C_{im}}{\partial t} = \alpha \, (C_m - C_{im}) - [\theta_m \, \mu_{l,im} + (1 - f) \rho_b \, k_d \, \mu_{s,im}] C_{im}$$

Eqn. 28

Application of the CXTFIT model

The excel based model, *CXTFIT,* solves the dimensionless MIM equations to simulate the

one-dimensional nonequilibrium transport of reactive and nonreactive solutes. *CXTFIT* is

predominantly designed to predict or fit breakthrough data from column tracer experiments.

Key advantages of this open-sourced code are its accessibility, readiness for modification and

its capability of solving both direct and inverse solutions for parameterization and prediction.

Within the *CXTFIT* program file, many user-designed functions are written in VBA code

to predict and analyze column flow tracer experiments. The MIM function initiates the

analytical solution for the nonequilibrium CDE which is further detailed by Eqn. 3.20 - 3.22 in

Toride's *CXTFIT Manual V2.0* (1995). The setup of *CXTFIT* incorporates input parameter cells for

dispersivity (λ [cm]), mobile water fraction (β [-]), mass transfer coefficient (ω [-]), and

retardation factor (R [-]), column length (L), average pore water velocity (cm/day), and pulse

duration (T_0) (Figure 6). Approximate values for λ, β, and ω were initially assigned to fit

experimental breakthrough curves. However, parameterization accuracy and efficiency was

improved by using a nonlinear least squares optimization code where parameters were

iteratively evaluated with the objective of minimizing the regression sum of squares (SSR) (Eqn.

14). Experimentally measured parameters such as column length (L [cm]), average velocity (v

[cm/d]), and pulse duration (T_o [-]) remained fixed during parameter optimization. Additionally,

statistical values such as the coefficient of determination (r^2) and root squared mean error

(*RMSE*) were calculated to evaluate the model fit accuracy (Eqn. 30 & 31).

$$SSR = \sum_{i=1}^{N}(C_i - f_i)^2 \qquad\qquad \text{Eqn. 29}$$

$$r^2 = 1 - \frac{SSR}{\sum_{i=1}^{N}(C_i - \bar{C})^2} \qquad\qquad \text{Eqn. 30}$$

$$RSME = \sqrt{\frac{\sum_{i=1}^{N}(C_i - f_i)^2}{N}} \qquad\qquad \text{Eqn. 31}$$

Equations 14, 15, and 16 were applied so that the measured or normalized (C/C$_o$)

effluent concentration were noted by C_i, predicted concentrations as f_i, the total number of

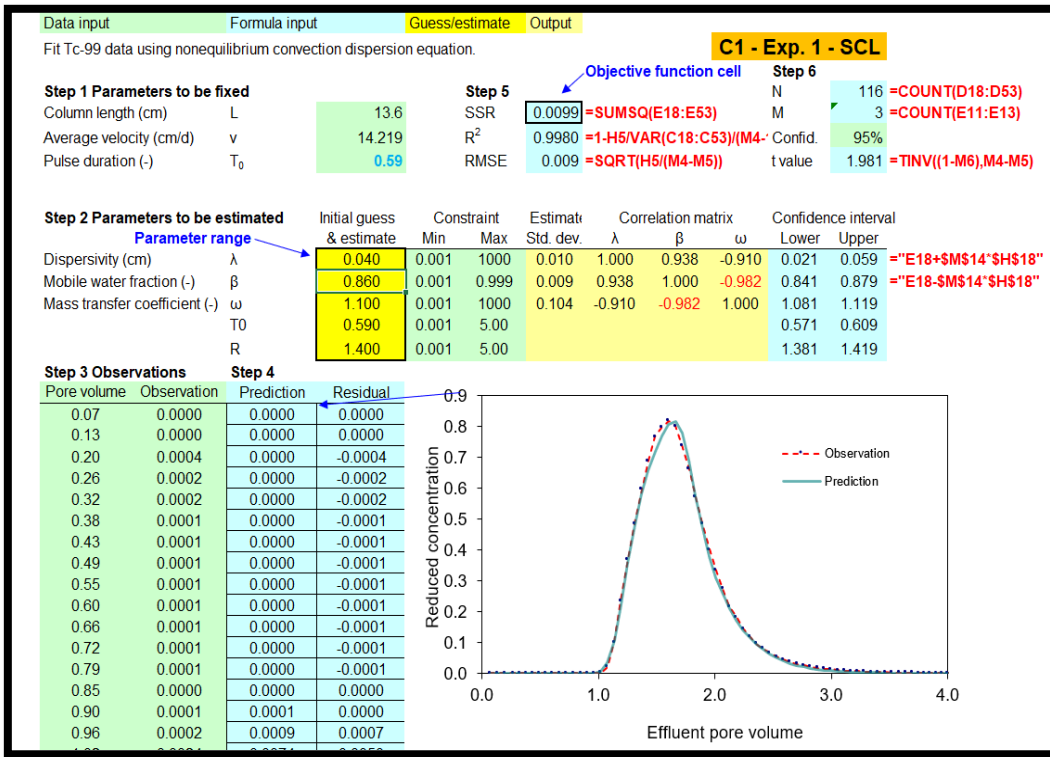data points as N, and the mean observed concentrations as $\bar{C}$.

Data input   Formula input   Guess/estimate Output

Fit Tc-99 data using nonequilibrium convection dispersion equation.   **C1 - Exp. 1 - SCL**

                Objective function cell

Step 1 Parameters to be fixed			Step 5						N	116	=COUNT(D18:D53)
Column length (cm)	L	13.6	SSR	0.0099	=SUMSQ(E18:E53)				M	3	=COUNT(E11:E13)
Average velocity (cm/d)	v	14.219	R^2	0.9980	=1-H5/VAR(C18:C53)/(M4-'				Confid.	95%	
Pulse duration (-)	T_0	0.59	RMSE	0.009	=SQRT(H5/(M4-M5))				t value	1.981	=TINV((1-M6),M4-M5)

Step 2 Parameters to be estimated		Initial guess	Constraint		Estimat	Correlation matrix			Confidence interval		
Parameter range		& estimate	Min	Max	Std. dev.	λ	β	ω	Lower	Upper	
Dispersivity (cm)	λ	0.040	0.001	1000	0.010	1.000	0.938	-0.910	0.021	0.059	="E18+M14*H18"
Mobile water fraction (-)	β	0.860	0.001	0.999	0.009	0.938	1.000	-0.982	0.841	0.879	="E18-M14*H18"
Mass transfer coefficient (-)	ω	1.100	0.001	1000	0.104	-0.910	-0.982	1.000	1.081	1.119	
	T0	0.590	0.001	5.00					0.571	0.609	
	R	1.400	0.001	5.00					1.381	1.419	

Step 3 Observations		Step 4		
Pore volume	Observation	Prediction	Residual	
0.07	0.0000	0.0000	0.0000	
0.13	0.0000	0.0000	0.0000	
0.20	0.0004	0.0000	-0.0004	
0.26	0.0002	0.0000	-0.0002	
0.32	0.0002	0.0000	-0.0002	
0.38	0.0001	0.0000	-0.0001	
0.43	0.0001	0.0000	-0.0001	
0.49	0.0001	0.0000	-0.0001	
0.55	0.0001	0.0000	-0.0001	
0.60	0.0001	0.0000	-0.0001	
0.66	0.0001	0.0000	-0.0001	
0.72	0.0001	0.0000	-0.0001	
0.79	0.0001	0.0000	-0.0001	
0.85	0.0000	0.0000	0.0000	
0.90	0.0001	0.0001	0.0000	
0.96	0.0002	0.0009	0.0007	

Figure 6 Parameter estimation template used by Excel based CXTFIT program

CHAPTER 4:   RESULTS

4.1   Pore-scale Imaging

Both vertical and horizontally oriented macropores were observed in all three wet-dry cycled SCL columns. Notably, imaging of column *SCL_M_2* revealed a vertical macropore structure extending from ~ 2 to 13 cm depth with a maximum diameter of ~ 1.5 mm (Figure 8). Connectivity of this structure throughout its ~12 cm length was proven to be continuous and meandering by examination of cross-sectional CT images through the Z axis (increasing sediment column depth) (Figure 9). No macropores were observed in wet-dry cycled sand columns (Figure 7). CT scans taken of SCL columns pre-wet dry cycling showed a homogeneous structure, confirming that packing methods did not induce the alterations observed post-exposure to a wet-drying event (Appendix, Figure 21-24).
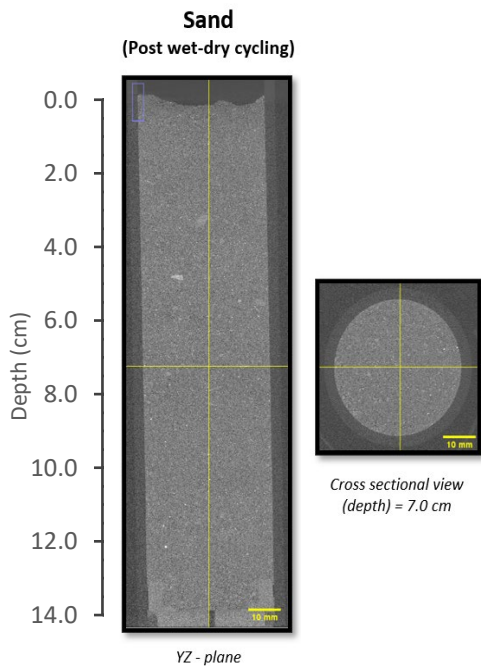

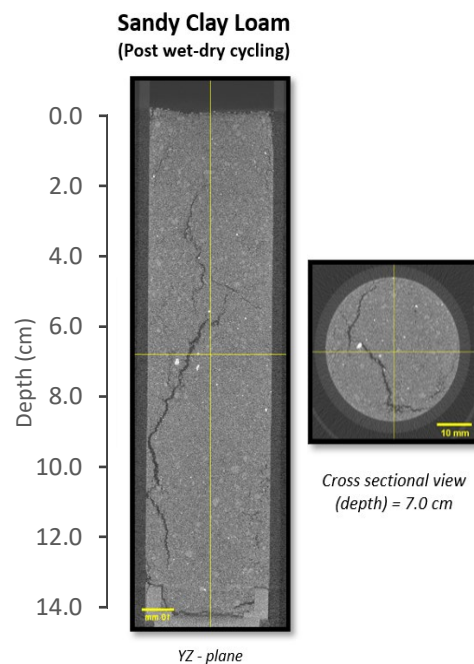Figure 7   YZ and XY orthogonal views of *SCL_M_2* taken from CT imaging post wet-drying

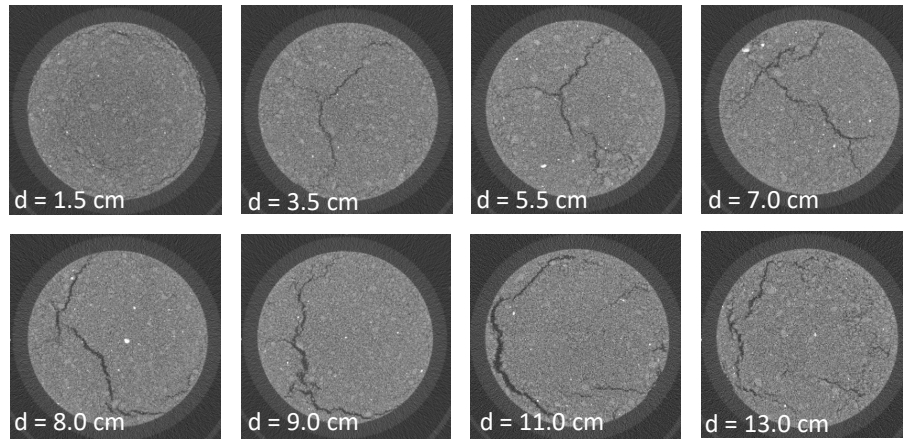Figure 8   YZ and XY orthogonal views of *S_M_2* taken from CT imaging post wet-dry cycling

Figure 9   CT images showing cross sectional views (XY plane) of column *SCL_M_2* increasing in depth (Z plane) from top left to top right. Scans show the connectivity of the vertical macropore network throughout the column

The *SCL_M_2* macropore network begins at an approximate depth of 2 cm where three symmetrical fractures converge (Figure 9). Increasing to a depth of 7 cm, the convergent cracks propagate vertically and form a "T" shaped fracture (in cross-section). The cracks then conform into a single fracture (d = 8 cm) that meanders towards the inner wall of the column. The fracture then closes at a depth of 13 cm as it approaches the column plug. Consistent with *SCL_M_2* imaging, the orientation of macropores in *SCL_M_1* and *SCL_M_3* were predominantly vertical and connected through the column.
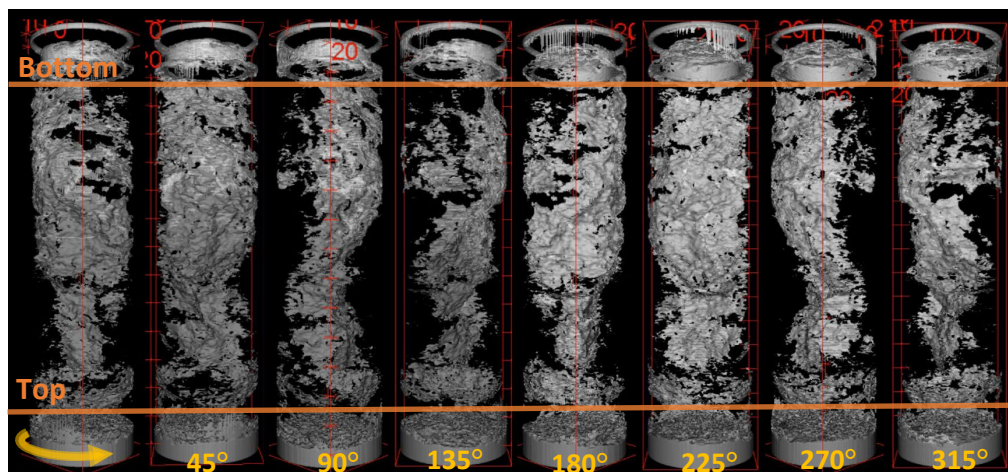

Figure 10   Three-dimensional reconstruction of macropore network in *SCL_M_2* (generated from CT imaging). Clockwise rotating views shown every 45°. Orange lines delineate macropore network (middle) from column apparatus (top and bottom)

4.2   Column Flow Experiments in Homogeneous Soils

Br and ^{99}*Tc Breakthroughs in Homogeneous Soils*

A preliminary unsaturated column flow experiment was completed to compare Br (a conservative tracer), ^{99}Tc, and ^{237}Np breakthroughs in columns packed homogeneously with SCL and sand sediment. During these experiments, no ponding occurred. In both column flow experiments (*SCL_H_1* and *S_H_1*), Br and ^{99}Tc breakthrough curves showed the similar shape and mean arrival times (MAT) respective to soil type (Figure 11). Br and ^{99}Tc mean arrival pore volumes (MAPV), calculated from the normalized first temporal moment (Eqn. 10, 11), were 1.63 and 1.61 for column experiment SCL_H_1 and 1.43 and 1.46 for S_H_1 (Table 5.1). Mean travel pore volume (MTPV) estimates for Br and ^{99}Tc, equivalent to the retardation factor (R), were 1.33 and 1.30 for SCL_H_1 and 1.07 and 1.08 for S_H_1. The remaining ^{99}Tc sorbed to SCL and sand-packed columns after column flow experiments were found to be at analytically insignificant concentrations.
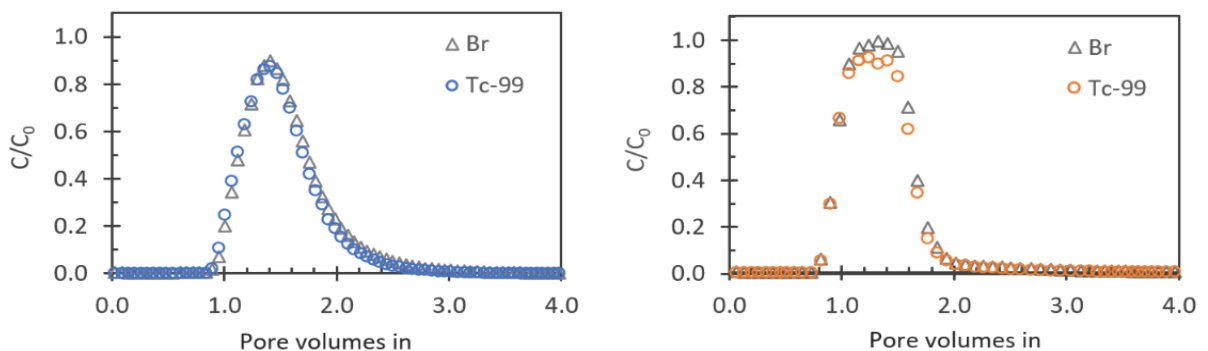

Figure 11   Br and ^{99}Tc breakthrough curves from columns *SCL_H_1* (Left) and *S_H_1* (Right) plotted as normalized concentration (C/C$_0$) vs. pore volumes added during column flow testing

Analysis of SCL soil and effluent samples from experiment *SCL_H_1* indicated 99% of the recovered ^{237}Np remained adsorbed to SCL soil after the experiment. In total, 7.6 pore volumes of water were flushed through the *SCL_H_1* column. Approximately 75% of the ^{237}Np in the SRS soil resided at depths between 2 – 6 cm (Figure 12). With a mean travel distance (MTD) of 4.6 cm, ^{237}Np travel velocity was calculated to be 1.6 cm d^{-1} (Table 5.4).

In experiment *S_H_1*, the column was homogeneously packed with sand. After flushing *S_H_1* with ~ 9 pore volumes of water, only 21% of the ^{237}Np injected remained adsorbed to the soil in the bottom 4 cm of the column. Sorbed ^{237}Np concentrations increased with depth to a maximum of 1.6 ng g-1 (Figure 12). Correspondingly, the ^{237}Np effluent pulse had a mean arrival time (MAT$_n$) of 2088 minutes (5.1 pv) and trended with a non-uniform profile and long tail that extended to the final time point (Figure 13).
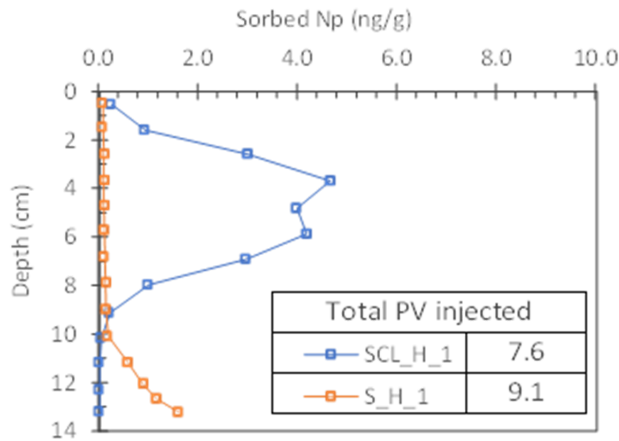
Figure 12   Sorbed ^{237}Np (ng g^{-1}) soil distributions from homogeneous SCL and sand experiments (*SCL_H_1, S_H_1*). Total number of pore volumes flushed through the column during respective experiments seen in table above.
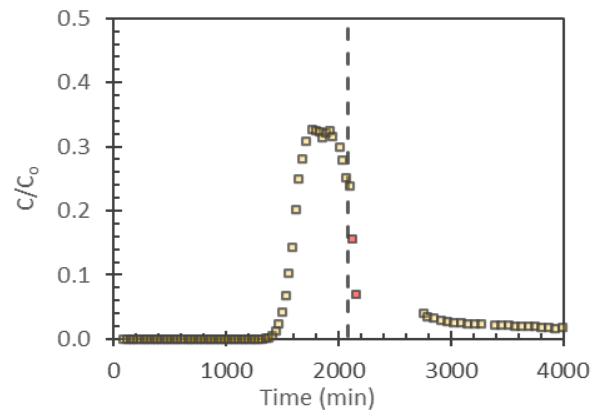
Figure 13 ^{237}Np elution curve from experiment *S_H_1* plotted as normalized concentration (C/Co) vs. elapsed time (min). Data points marked in red indicate compromised effluent samples. Loss of effluent samples occurred from 2200 through 3700 minutes

4.3 Column Flow Experiments in Wet-dry Cycled Soils

Column flow experiments completed on wet-dry cycled columns packed with sand or sandy clay loam soils were conducted in experiments *M_1 - 3.* Discussed further in *Ch. 4 Sect. 1*, macropores were visible in CT scans of columns *SCL_M_1-3* post-wet-dry cycling but not in sand columns *S_M_1 – 3*. For *M_1* column flow experiments, the average water content directly before the spike addition was ~ 0.1, while experiments *M_2* and *M_3* were initiated with an initial water content of ~ 0.25.

99-Technecium Breakthrough in Wet-Dry Cycled soils

MAPV calculations for ^{99}Tc in SCL experiments *M_1*, *M_2*, and *M_3* were 1.74, 1.73, and 1.66, while MAPV values in corresponding sand experiments were 1.45, 1.60, and 1.49 (Table 5.1). The total number of pore volumes flushed through each column ranged from 7.6 – 6.8 in SCL and 9.1 to 7.0 in sand (Table 5.4). Coinciding with results in homogeneous soils, ^{99}Tc was not found sorbed to sand or sandy clay loam sediments analyzed after column flow experiments.

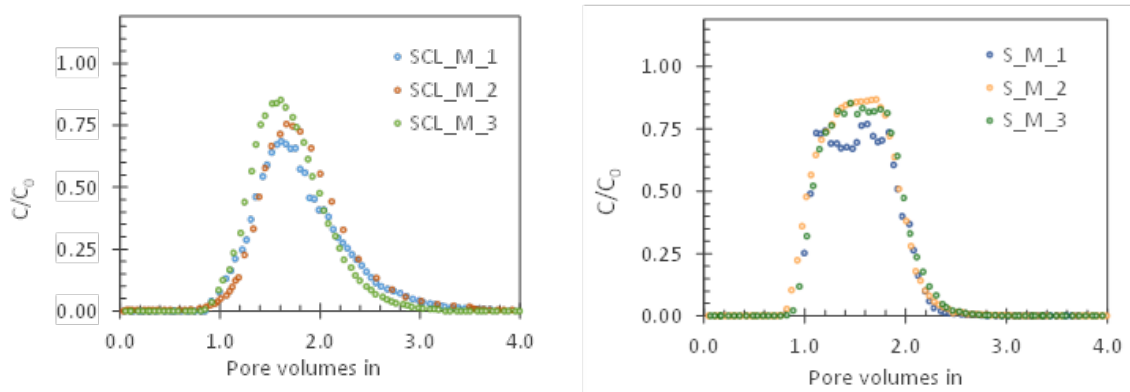Figure 14   C/C$_0$ (^{99}Tc) plotted against pore volumes injected during unsaturated column flow experiments on sandy clay loam (left) and sand (right) sediments varying in heterogeneity

^{237}Np was not detected at analytically significant concentrations in effluent samples across all macropore experiments. In SCL experiments *M_1* and *M_3,* mean travel distances (*MTD*) were 2.6 and 2.0 cm, with resulting contaminant velocities (v_c) of 1.0 and 0.8 cm d^{-1} (Table 5.4). Contaminant velocities ^{237}Np were determined by dividing the mean travel distance (MTD) by the total elapsed time during the column flow experiment. In corresponding sand experiments (*S_M_1* and *S_M_3*), ^{237}Np MTD values were 1.2 and 2.3 cm. Resulting v_c values were 0.5 and 1.0 cm d^{-1}.
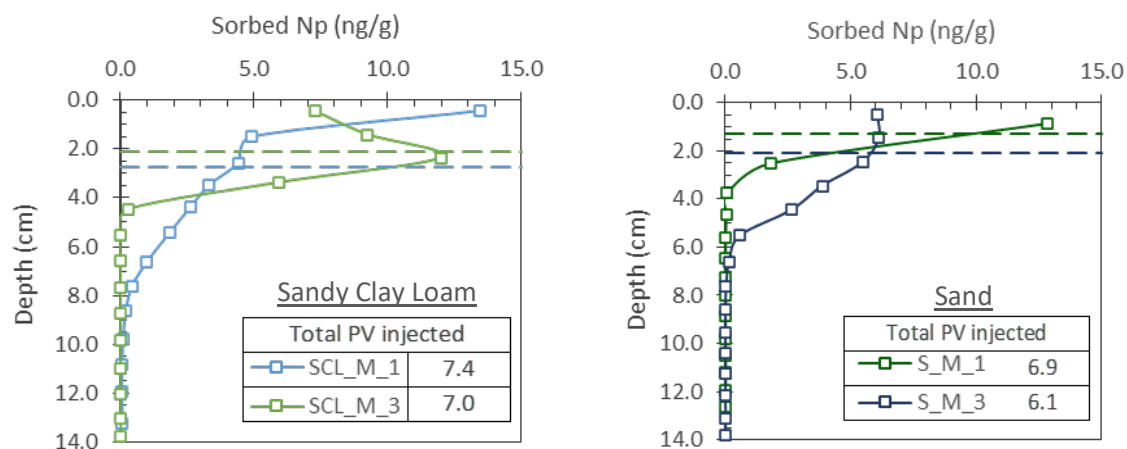
Figure 15   Sediment ^{237}Np concentration (ng g^{-1}) profiles acquired by sectioning experimental sediment columns. ^{237}Np migration relative to the total number of pore volumes flushed through the column (see legend). Dashed lines indicate the mean travel distance (MTD) for respective experiments

4.4   Effluent pH

The pH of the spike solution in the preliminary column flow experiment (*SCL_H_1* and *S_H_1*) was 3.0. Resulting effluent pH values for *SCL_H_1* were averaged at 4.8 while S_H_1 effluent pH averaged at 5.1. Over the duration of experiment 1, the pH of *SCL_H_1* effluent exponentially dropped from 7.3 to 4.4 over the first 17 hours (2.1 PV) (Figure 16). Effluent pH for *SCL_H_1* remained stable at 4.5 for the final ~ 4 pore volumes. The pH of *S_H_1* effluent

remained stable at ~ 6.1 for the first 10 hours (2.3 pv) of the experiment. Over the following 1.7

pore volumes (pv), pH dropped steadily from 6.5 to 4.5, where it remained stable.

The spike solution used in experiment *M_1-3* measured to a pH of 5.6. The overall trend of

effluent pH measurements taken throughout macropore experiments was consistent respective

to soil type. For sand-packed columns (*S_M_1-3*), pH measurements remain consistent at ~ 6.1

from 0 to 4 PV, then decrease at an average rate of 0.3 pH per pv for the remainder of the

experiment (Figure 16).
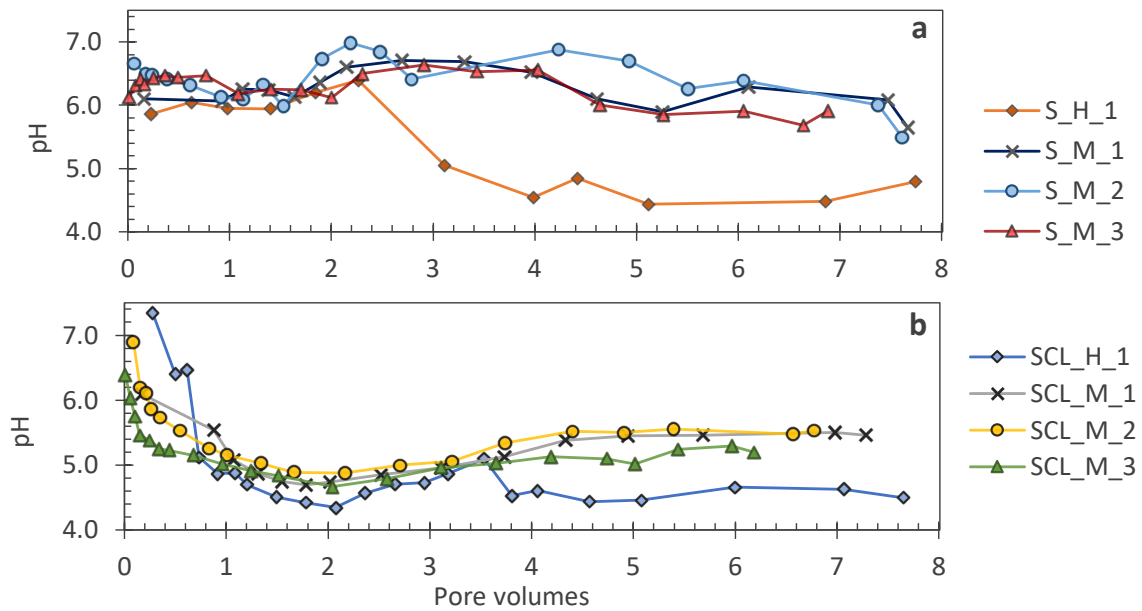

Figure 16   Effluent pH measurements taken from sand (16a) and SCL (16b) column flow experiments plotted

4.5   Flowrate

Across all column flow experimental datasets, flow rate measurements varied with standard deviations ranging from 8E-3 to 2E-2 mL min^{-1} (RSD = 7 to 18%). Notably, recorded effluent flow rates for *SCL_M_2* and *S_M_2* dropped from ~ 0.09 to ~ 0.06 mL min^{-1} and remained stable at that minimum rate for a span of 660 minutes (540 to 1200 min). (Appendix, Figure 25). With a mean flow rate ($\bar{Q}$) of 0.085 and 0.089 mL min^{-1} for *SCL_M_2* and *S_M_2*, deviations increased the RSD to 18.9% and 18.2%, respectively (Table 4.1). Flowrate deviations are suspected to be caused by improper potentiometer settings of the peristaltic pump. Flowarate deviations for all experiments except for *SCL_M_1*, S_*M_1* and *S_H_1* were less than 13% (Table 4.1).

Table 4.4   Column Flow Experiments: Flow Rate Variability

Column ID	$\bar{Q}$,[a] mL min^{-1}	$\bar{Q}_{inj}$,[b] mL min^{-1}	SD$_Q$,[c] mL min^{-1}	RSD$_Q$,[d] %
Homogenous				
SCL_H_1	1.1×10^{-1}	1.2E-01	0.8E-2	7.2
S_H_1	1.1E-01	9.6E-02	1.7E-2	15.9
Wet-dry cycled				
SCL_M_1	9.3E-02	8.4E-02	1.2E-2	12.6
SCL_M_2	8.5E-02	8.9E-02	1.6E-2	18.9
SCL_M_3	9.5E-02	9.5E-02	0.6E-2	6.5
S_M_1	9.3E-02	8.8E-02	1.1E-2	11.9
S_M_2	8.9E-02	9.5E-02	1.6E-2	18.2
S_M_3	9.8E-02	9.0E-02	0.8E-2	8.5

[a] Average volumetric flowrate ($\bar{Q}$) calculated by the arithmetic mean of *Q(t)* from t_0 to t_f. For each experimental dataset, *Q(t)* was determined volumetrically from fraction collected effluent samples
[b] Average volumetric flowrate during spike injection
[c] Volumetric flowrate variance about the mean flowrate ($\bar{Q}$)
[d] Percent standard deviation determined relative to the mean volumetric flowrate (RSD = $\frac{SD}{\bar{Q}}$ * 100)

4.6   Mass Balances

Bromide and ^{99}Tc recoveries were determined by comparing M_{t_out}, the mass output

calculated as $\int \frac{c}{c_0} dt$ [t], to M_{t_in}, equivalent to the pulse duration in units of time. This analysis

evaluates the mass balance in units of time under the assumption that flowrates remained

constant during the injection of the spike. Further explanation of this analysis is provided in *Ch.*

3 sect. 3.3. Recoveries of ^{99}Tc ranged between 88% to 108% across all experiments (Table 4.2).

[237]Np recoveries, calculated directly from sorbed concentrations, ranged from 87% to 98% in

SCL experiments and 74% to 77% in sand.

Table 4.5   Measured Experimental Parameters and Effluent Mass Balance

Column ID	V_{pore} mL	T_0 -	Mass in [a] M_{t_in} min Br	[99]Tc	Mass out [b] M_{t_out} min Br	[99]Tc	Recovery [c] % Br	[99]Tc
Homogeneous								
SCL_H_1	57.1	0.62	354.1	354.1	351.1	347.0	99	102
S_H_1	47.5	0.77	310.1	310.1	292.6	284.5	94	93
Wet-dry cycled								
SCL_M_1	50.0	0.78	-	405.5	-	396.0	-	98
SCL_M_2	53.5	0.80	-	481.3	-	517.6	-	108
SCL_M_3	53.9	0.80	-	462.0	-	416.0	-	90
S_M_1	46.5	0.93	-	405.0	-	420.5	-	104
S_M_2	49.2	0.87	-	504.4	-	535.3	-	106
S_M_3	49.3	0.85	-	462.0	-	405.3	-	88

[a] Mass injected determined from initial spike concentrations and measured volumetric flow rates.
[b] Total mass recovered from effluent in units of time ($M_{t\_out} = \mu_0 = \int \frac{c}{c_0} dt \ [T]$) where effluent
concentrations, normalized by the spike concentration, are integrated with respect to time.
[c] Recovery calculated by dividing the mass output, measured in units of time, by t_0, the mass input
equivalence *(Recovery = $M_{t\_out} * M_{t\_in}^{-1} = \int \frac{c}{c_0} dt * t_o^{-1}$)*

CHAPTER 5:   DISCUSSION

5.1   Impacts of Macropores on Tc-99 Transport

Mean Arrival

Results from this study show that macropore structure present in sandy clay loam soils had no statistically significant impact on the mean arrival of ^{99}Tc in unsaturated flow conditions. ^{99}Tc retardation factors were 1.30 in homogeneous SCL and ranged between 1.28 and 1.41 in SCL experiments with macropores. The initial breakthrough pore volumes (IBPV), the pore volume injected at which 1% of the solute has eluted, slightly decreased in both SCL and sand experiments for ^{99}Tc. The IBPV was 1.08 in homogeneous SCL and ranged between 0.92 and 1.0 in SCL experiments with macropores (Table 5.1). This indicates that shorter flow paths may be more active in macroporous soils but further experimentation with more accuracy is needed to

Table 5.6   Temporal Moments Analysis of Br and ^{99}Tc Breakthrough Data

Column ID	MAT$_n$,[a] min		MAPV,[b] -		MTT,[c] min		MTPV,[d] -		IBPV[e] -
	Br	^{99}Tc	Br	^{99}Tc	Br	^{99}Tc	Br	^{99}Tc	^{99}Tc
Homogeneous									
SCL_H_1	883.3	862.9	1.63	1.61	717.8	697.4	1.33	1.30	1.08
S_H_1	652.9	628.6	1.43	1.46	487.2	476.3	1.07	1.08	0.95
Wet-dry cycled									
SCL_M_1	-	935.0	-	1.73	-	730.5	-	1.35	0.92
SCL_M_2	-	1164.1	-	1.74	-	1006.3	-	1.41	0.94
SCL_M_3	-	1005.6	-	1.66	-	775.3	-	1.28	1.0
S_M_1	-	726.8	-	1.45	-	522.3	-	1.04	-
S_M_2	-	909.7	-	1.60	-	632.2	-	1.12	0.85
S_M_3	-	811.2	-	1.49	-	580.2	-	1.07	0.88

[a] Normalized mean arrival time (*MAT$_n$*), or mean residence time (*t$_m$*), representing the time corresponding to a breakthrough curve's center of mass ($MAT = \mu_1' = \frac{\mu_1}{\mu_0}$; $\mu_1 = \int \frac{C}{C_0} t\, dt$; $\mu_0 = \int \frac{C}{C_0} dt$)

[b] Mean arrival pore volume (*MAPV*), converted from MAT$_n$, with the average volumetric flow rate ($\bar{Q}$) and pore volume measurements *(MAPV = MAT$_n$ * $\bar{Q}$ * V$_{pore}$$^{-1}$)*

[c] Mean travel time (*MTT*) calculated from the *MAT$_n$* minus the average injection time ($MTT = MAT – 0.5 * t_0$)

[d] Mean travel pore volume, equivalent to retardation factor (*R*), converted from *MTT* to units of pore vol. inj.

[e] Initial breakthrough pore volume defined as the # of pore volumes inj. corresponding to elution of 1% of the solute

make this claim. Macropores were not observed in sand packed columns post wet-dry cycling; thus, definitive conclusions relating macropore structures and ^{99}Tc mobility in sand cannot be made. However, ^{99}Tc retardation factors were consistent across homogeneous sand and wet-dry cycled sand experiments and IBV also decreased in sand columns exposed to a wet-drying event (Table 5.1).

Mobile Water Fraction

Macropore structures in SCL soils showed no statistically significant impacts for MIM estimated mobile water fractions (β). The mobile water fraction parameter accounts for the stratification of a soil matrix into mobile and stagnant fluid regions (conditions of non-equilibrium). In this model, transport is governed by the convection dispersion equation in mobile regions and by the rate of exchange between regions (mass transfer coefficient) in immobile regions. The mobile water fraction term controls the degree to which transport is partitioned by either equilibrium or non-equilibrium transport processes. It assumes that when $\beta = 1$ the CDE is restored and if β drops below 1, nonequilibrium conditions are introduced.

Mobile water fractions estimated from ^{99}Tc breakthrough were 0.90 ± 0.02 and 0.92 ± 0.03 in homogeneous SCL and sand experiments (Table 5.3). CDE ($\beta = 1$, $\lambda = 0.15$ cm, R = 1.4) describes ^{99}Tc breakthrough for *SCL_H_1* with a best fit R^2 of 0.968; however, MIM predictions ($\beta = 0.90$, $\lambda = 0.08$ cm, $\omega = 0.65$, R = 1.41) fit ^{99}Tc breakthrough with an R^2 of 0.997 (Figure 17). Based on R^2 fit estimates, better curve fitting was acquired with MIM for all sand experiments as well. These results suggest that in homogeneously packed SCL and sand, unsaturated flow conditions reduce the number of flow paths and induce nonequilibrium flow and transport, supporting claims by Padilla (1999).
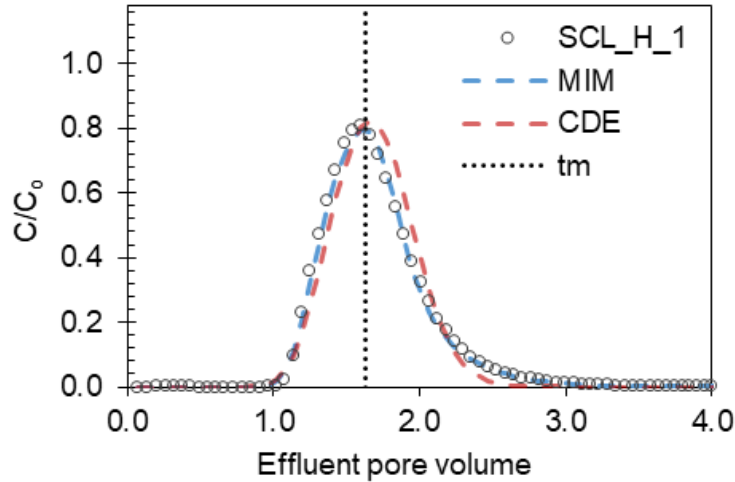
38

Figure 17   Comparison of CDE and MIM best fits to SCL_H_1 [99]Tc
breakthrough plotted as C/Co vs. effluent pore volumes. (CDE R2 = 0.968,
MIM R2 = 0.997)

Dispersivity

Although ^{99}Tc mean arrivals were not significantly impacted, dispersivity (λ) in wet-dry

cycled SCL and sand soils increased relative to breakthrough curves in respective homogeneous

soils (Figure 18). Dispersivity, estimated with the nonequilibrium convection-dispersion

equation (MIM), were fit to experimental data with R^2 values ranging from 0.933 to 0.997. MIM

estimates of ^{99}Tc dispersivity in homogeneous SCL were 0.08 ± 0.02 cm while dispersivity for

macroporous SCL experiments *M_1*, *M_2*, and *M_3* were 0.26 ± 0.1, 0.19 ± 0.04, and 0.21 ±

0.05 cm (Table 5.3). Variance, the second temporal moment indicative of plume spread, also

increased in all wet-dry cycled SCL and sand flow experiments relative to homogeneous

experiments (Figure 19).

MIM best fits of λ for ^{99}Tc in sand showed no statistically significant deviations in wet-

dry cycled experiments. However, variance, determined via temporal moments analysis,

increased from homogeneous sand to wet-dry cycled sand experiments (Table 5.2).
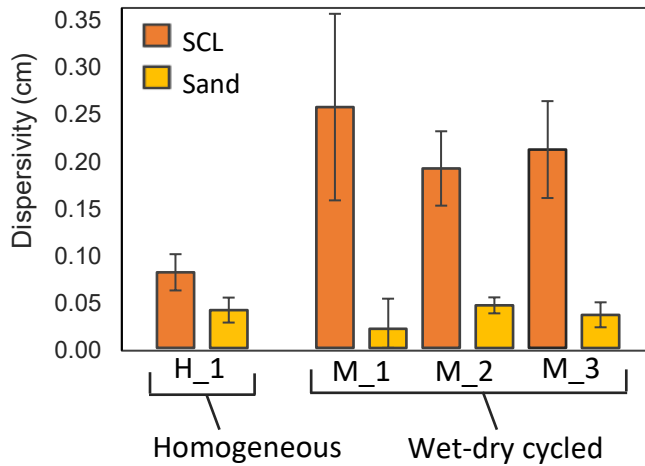
Figure 18 Comparison of ^{99}Tc dispersivities in homogeneous (*H_1*) and wet-dry cycled (*M_1 – 3*) SCL and sand. Dispersivity determined from MIM best fits for unsaturated SCL and sand column flow experiments.

Increases in dispersivity of ^{99}Tc in macroporous SCL soils are attributed to increased fluid mixing during transport and capillary exclusion. Effectively, solute mixing in porous media is controlled by travel distances, tortuosity, and spatial variations in flow velocity. Unsaturated fractures throughout the matrix act as capillary barriers, either isolating transport to subsections of the matrix (vertical macropores) or blocking flow and infiltration (horizontal macropores). Column flow studies conducted in homogeneous soils by Padilla (1999) suggest that in unsaturated conditions, dispersivity is indirectly proportional to water content. Padilla asserts that as water content decreases below saturation, the number of flow paths decrease and pore-water velocity variations increase, effectively increasing solute dispersivity. In this study, breakthrough curves indicate that increases in ^{99}Tc dispersivity are related to analogous processes (velocity variations and tortuosity) but is induced by increasing macroporosity.
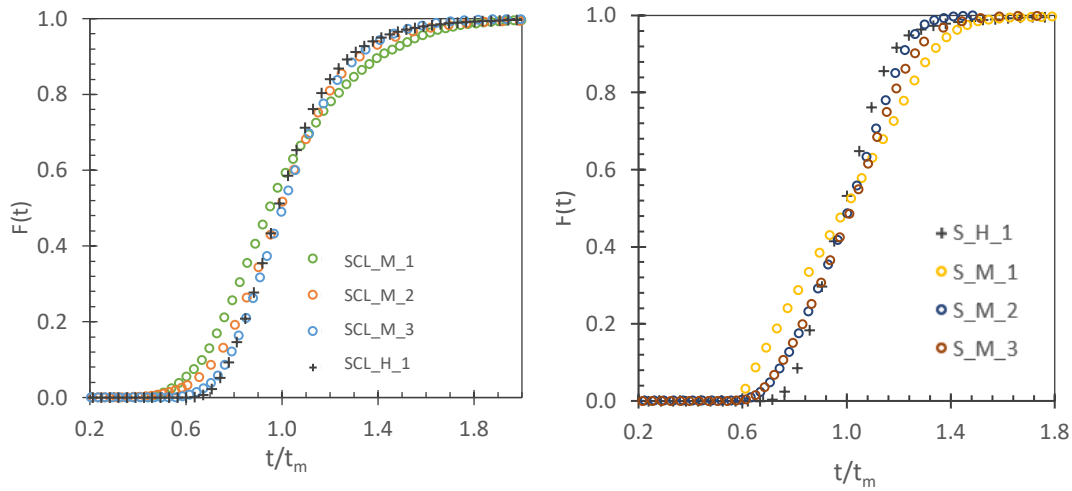
Figure 19 ^{99}Tc cumulative distribution curves (*F(t)*) plotted vs. dimensionless time for column flow experiments in homogeneous and wet-dry cycled soils. $F(t) = \int E(t)\,dt$ and *T = t/t$_m$* where *t* is time and t_m is the first temporal moment (solute mean arrival time)

Table 5.7   Temporal Moments with Variable Flowrate

	Temporal Moments (Br and Tc-99)				
ID	1st moment [a], t_m min		Variance [b], σ min^2	Skewness [c], *SK* min$^{3/2}$	
	Br	^{99}Tc	^{99}Tc	^{99}Tc	
Homogeneous					
SCL_H_1	852.5	862.9	31740	1.20	
S_H_1	621.7	626.1	8445	0.89	
Wet-dry cycled					
SCL_M_1	-	929.2	64798	0.59	
SCL_M_2	-	1167.9	74712	0.80	
SCL_M_3	-	1007.6	44258	0.77	
S_M_1	-	736.0	34483	0.34	
S_M_2	-	909.9	41077	0.28	
S_M_3	-	811.6	25470	0.28	

[a] Mean residence time (t$_m$) calculated as $t_m = \int t * E(t)dt$ where $E(t) = \dfrac{C_{out}(t)Q}{\int_0^\infty C_{out}(t)Q\,dt}$

[b] Variance indicating the degree of spreading

[c] Skewness indicating the extent of asymmetry

Table 5.8   1D Nonequilibrium CDE (MIM): Parameter Estimation

ID	Input Parameters				Estimated Model Parameters						
	L	v	T_o	R	λ [a]	±	β [b]	±	ω [c]	±	R^2
	cm	cm d^{-1}	-	-	cm		-		-		
Homogeneous											
SCL_H_1	13.6	14.61	0.62	1.41	0.08	0.02	0.90	0.02	0.65	0.05	0.997
S_H_1	13.5	14.62	0.77	1.14	0.04	0.01	0.92	0.03	0.79	0.72	0.992
Wet-dry cycled											
SCL_M_1	14.2	12.42	0.78	1.33	0.26	0.10	0.85	0.05	0.65	0.41	0.992
SCL_M_2	14.1	11.32	0.80	1.44	0.19	0.04	0.87	0.02	0.63	0.24	0.996
SCL_M_3	14.1	12.69	0.80	1.40	0.21	0.05	0.88	0.03	0.65	0.35	0.996
S_M_1	14.1	12.38	0.93	1.36	0.02	0.03	0.88	0.07	0.88	1.67	0.933
S_M_2	13.5	11.91	0.87	1.15	0.05	0.01	0.89	0.01	0.80	0.55	0.997
S_M_3	14.1	13.10	0.85	1.17	0.04	0.01	0.90	0.02	0.88	0.46	0.997

[a] Dispersivity [cm]

[b] Mobile water fraction [-]

[c] Mass transfer coefficient [-]

5.2   Impacts of Macropores on Neptunium-237 Transport

[237]Np travel velocities increased on average by 53% in homogenous SCL when compared to macroporous SCL. Travel velocity estimates were 1.6, 1.0, 0.8 cm d-1 for *SCL_H_1, SCL_M_1,* and *SCL_M_3*. This increase in [237]Np mobility is attributed and increase in the spike solution pH differences from homogenous and heterogeneous experiments. As discussed in *Ch. 4 sect. 4*, the spike pH was 3.0 in homogeneous sand and SCL experiments and 5.6 in heterogenous experiments. Powell (2018) shows that the [237]Np sorption is fully reversible and dependent on pH. In Powell's desorption experiments using similar SCL soils collected from SRS, [237]Np fraction sorbed (%) is ~ 100% at a pH of 8.5, ~ 15% at a pH of 5.5, and < 5% at a pH of 4.6 (Powell, 2018).

Reactive kinetic transport simulations (PHREEQC) were run to assess how pH differences between homogenous and heterogeneous SCL experiments impacted [237]Np mean travel distances. The 1D transport model was comprised of 50 cells which cumulatively spanned 14

cm. The simulation was run for a total of 1000 shifts with each shift equivalent to a time step of 600 seconds. Assuming a 50 mL pore volume, every 50 shifts is equivalent to 1 pore volume of water run through the model domain.

Table 5.9   Sorbed Np-237: Spatial Moments Analysis and Mobility Characteristics

ID	Experimental Measurements			Spatial Moments Analysis (^{237}Np)				
	pH_{spike}	$\overline{pH}_{effluent,}$ [a]	Total PV$_{inj}$	$x_{m,}$ [b]	MTD, [c]	$v_{c,}$ [d]	R, [e]	
				cm	cm	cm d^{-1}	-	
Homogeneous								
SCL_H_1	3.0	4.9	7.6	4.9	4.6	1.6	9.3	
S_H_1	3.0	5.1	9.1	-	-	10.3	4.2	
Wet Dry - Cycled								
SCL_M_1	5.5	5.2	6.9	2.8	2.6	1.0	12.2	
SCL_M_2	5.5	5.3	6.6	-	-	-	-	
SCL_M_3	5.5	5.1	6.1	2.1	2.0	0.8	16.5	
S_M_1	5.5	6.2	7.4	1.3	1.2	0.5	22.0	
S_M_2	5.5	6.4	7.0	-	-	-	-	
S_M_3	5.5	6.2	7.0	2.5	2.3	1.0	14.0	
PHREEQC	Model Input Parameters							
Sim_1	-	4.9	7.6	4.8	4.6	1.5	9.5	
Sim_2	-	5.2	6.9	0.6	0.6	0.2	66.7	

[a] pH averaged over the full duration of respective column experiments as $\int pH\,Q(t)\,dt\,\bar{Q}^{-1}$

[b] Normalized first spatial moment (center of mass) calculated as $x_m = \dfrac{\int C(x)\,x\,dx}{\int C(x)\,dx}$

[c] Mean travel distance [cm] determined by $MTD = x_m - (0.5 * t_0 * v_c)$

[d] Contaminant velocity [cm d^{-1}] where $v_c = x_m * t_{final}$

[e] Retardation factor defined as the ratio between v_w *(tracer velocity)* and v_c $(R = \dfrac{v_w}{v_c})$

PHREEQC simulations run with porewater pH fixed at 4.9 estimated the ^{237}Np MTD to be 4.8 cm, within 0.1 cm of experimental results, after flushing with 7.6 pore volumes (Table 5.4). This simulation was rerun with a fixed pH of 5.2, equivalent to the average pH of effluent in heterogenous SCL experiments which estimated that ^{237}Np mean travel distances would be 0.01 cm (Figure 20). These simulations indicate that ^{237}Np transport is largely dependent on pH, thus, accurate comparisons of ^{237}Np transport in homogeneous and wet-dry cycled soils cannot be made.
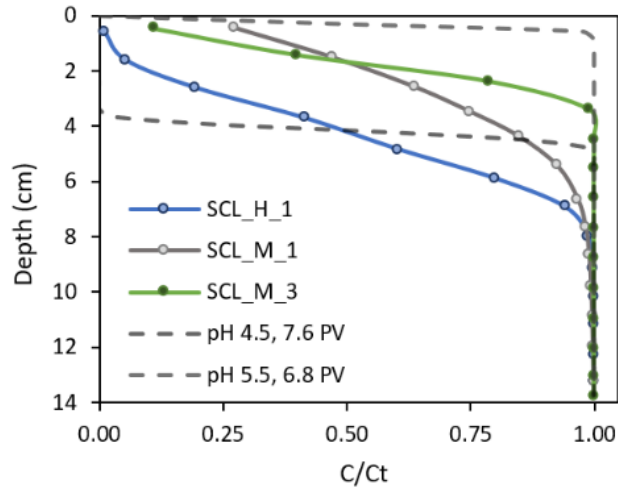
Figure 20   Comparison of [237]Np soil distributions for homogeneous and macroporous SCL. Dashed lines correspond to PHREEQC simulated estimates of [237]Np transport in SCL. Simulations were run varying only pH (pH = 4.9, pH = 5.5)

5.3   Comparison and Implications of Br and Tc-99 Breakthrough

Due to analytical difficulties, bromine was not added as a tracer for wet-dry cycled SCL and sand column flow experiments; however, results from preliminary experiments in homogeneous soils showed that Br and ^{99}Tc have similar mobilities in both experimental soil types. Bromide retardation factors in homogenous SCL and sand experiments were found to be 1.33 and 1.07. Retardation factors for ^{99}Tc were 1.30 and 1.08 for these same experiments (Table 5.1). Furthermore, plume spreading, and peak shapes were nearly identical respective to soil types (Figure 11). Corresponding R measurements between Br (non-reactive tracer) and ^{99}Tc breakthroughs suggest that ^{99}Tc should be considered non-reactive to produce precautionary transport estimates.

CHAPTER 6:   CONCLUSIONS

This study finds that in unsaturated conditions, macropore structure in SCL soils increases ^{99}Tc dispersivity estimates. However, mean arrivals of ^{99}Tc were not impacted by macropore structures present in SCL soils. The retardation factor determined from unsaturated column flow experiments for ^{99}Tc were 1.30 in homogeneous SCL and 1.35, 1.41, and 1.28 in macroporous SCL. Exposing SCL soil to a wetting and drying event proved to generate macropores in all exposed SCL columns. Macropores visible in SCL soil were predominantly vertical. We conclude that macropores can facilitate capillary exclusion in unsaturated macroporous soils. In this process, cracks create capillary barriers separating the matrix into mobile fluid and immobile regions, which increases the spatial variability of flow velocities dependent on macropore orientation (faster if vertically oriented and slower if horizontal).

CT scans of sand-packed columns showed no indications of macropore formation post-exposure to wet-dry cycling; however, breakthrough and IBPV increased in macroporous experiments increased, suggesting that macropores may be present but were not visible in CT scans. Retardation factors for ^{99}Tc were similar between exposure groups. Homogeneous sand ^{99}Tc R was estimated to be 1.08, while in wet-dry cycled experiments, estimates were 1.04, 1.12, and 1.07. Large uncertainties in parameters estimated from MIM predictions data presented challenges when interpreting mobile water fraction (β) and mass transfer coefficients (ω).

Accurate comparisons of ^{237}Np transport in homogeneous and wet-dry cycled SCL and sand could not be made due to variations in influent pH across experiments. With an average effluent pH of 4.9, the mean travel distance (MTD) for ^{237}Np was 4.8 cm ($K_d = 1.7$ cm^3 g^{-1}). In

macroporous experiments, the average pH was 5.4 resulting in SCL MTD's of 2.6 and 2.0 cm

(SCL_M K_d = 2.2, 3.0 cm^3 g^{-1}). Sand experiments showed similar trends, with K_d estimates

increasing from 0.7 cm^3 g^{-1} in homogeneous experiments (average effluent pH = 4.9) to 4.3 and

2.5 cm^3 g^{-1}. PHREEQC 1D transport simulations (CDE) run at fixed pH's of 4.9, and 5.2 showed

that dropping the pH in these ranges increased the mean travel distance from 0.1 to 4.9 cm

(Fig. 14). PHREEQC simulations support claims that the dominant factor affecting [237]Np mobility
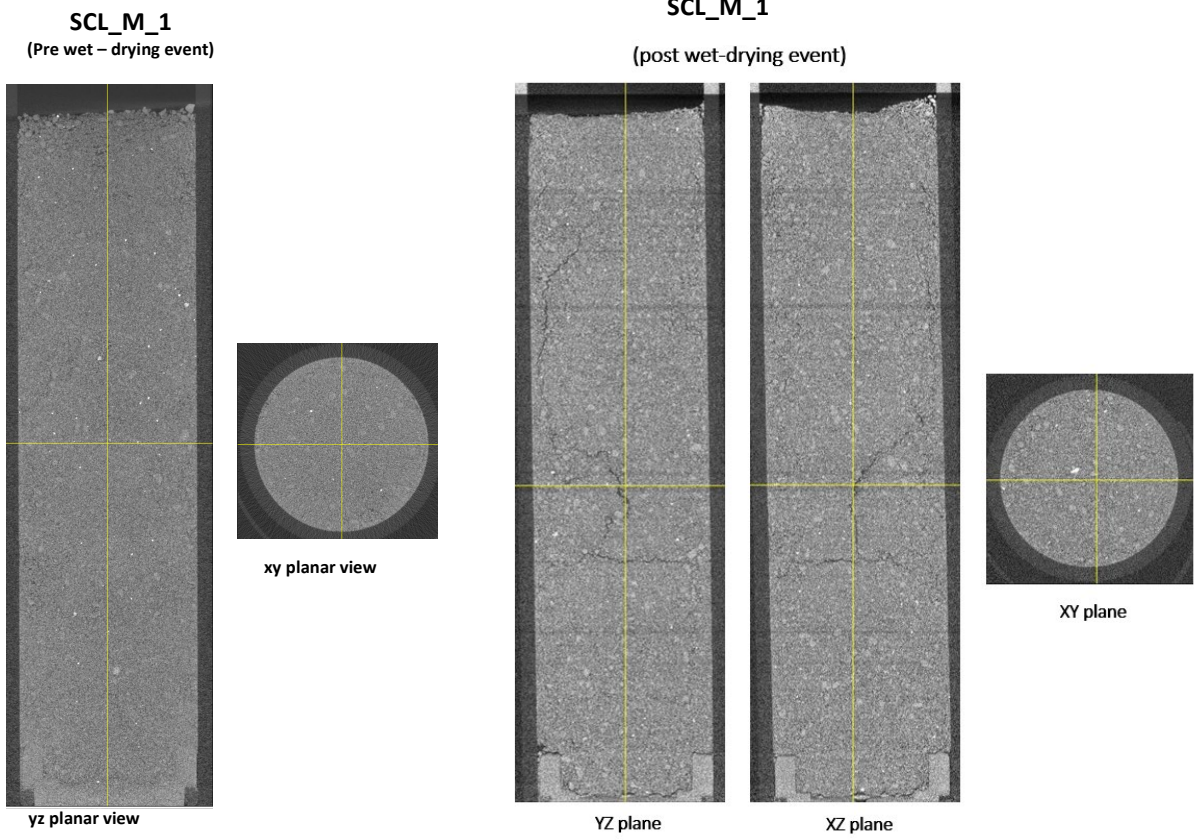
across these experiments is pH.

APPENDICES

Figure 21   CT imaging of SCL_M_1 Pre (left) and post (right) wet - drying event (YZ, XZ, and XY planar views)

SCL_M_3
(Post wetting – drying event)

7 mm

7 mm

xy planar view
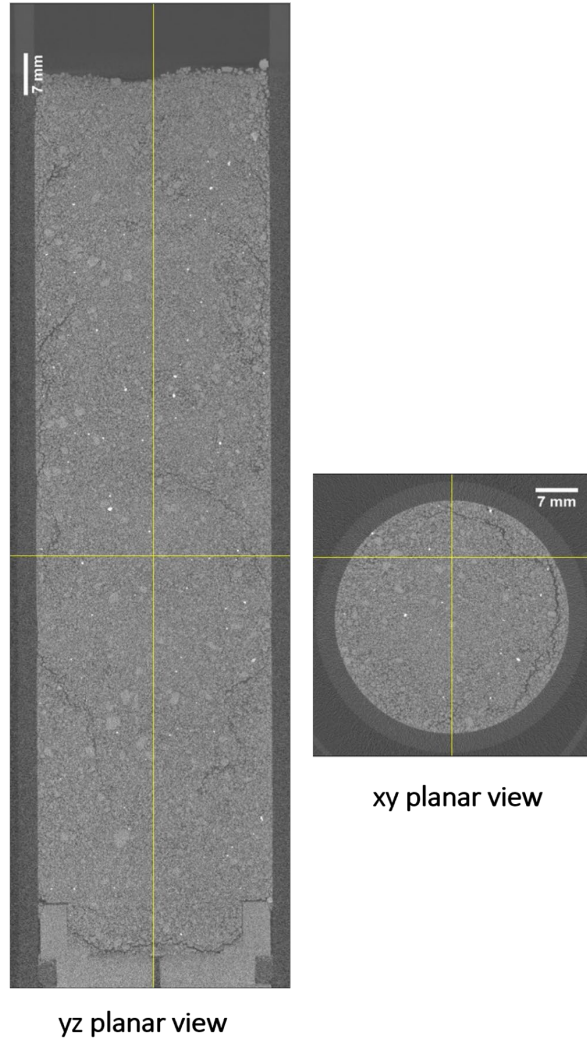
yz planar view

Figure 22   CT imaging of SCL_M_3 post wet-drying event

SCL_M_2
(Post wet – drying event)

xy planar view
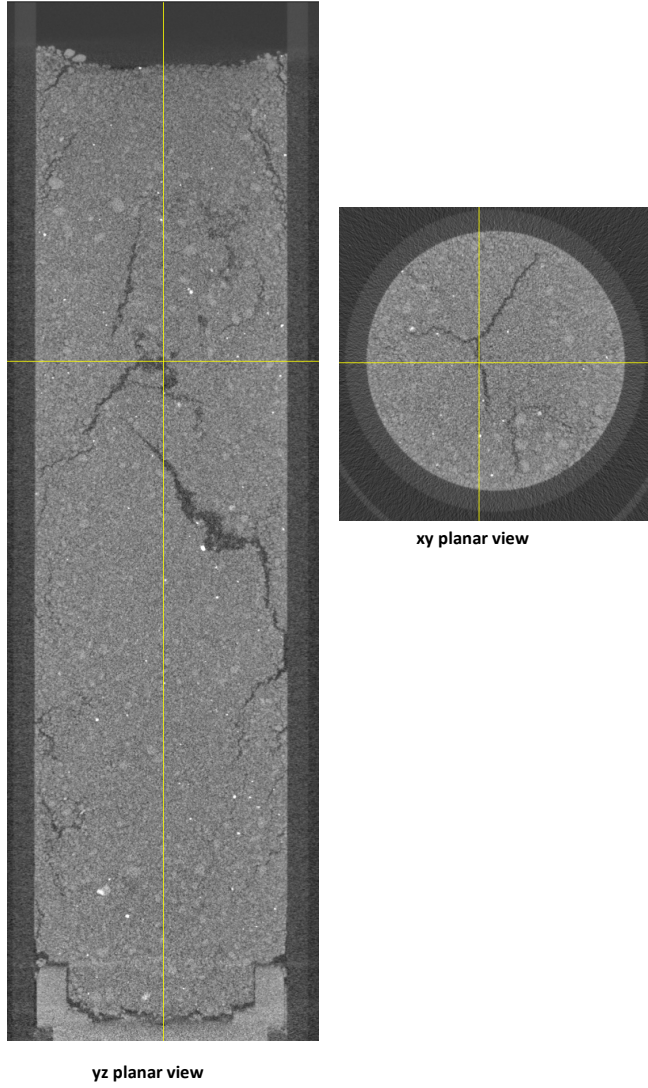
yz planar view

Figure 23   CT imaging of SCL_M_2 post wet-drying event

S_M_1
(Pre wet – drying event)

xy planar view

yz planar view

S_M_1
(Post wet-drying event)

xy planar view

yz planar view

Figure 24   CT imaging of S_M_1 Pre (left) and post (right) wet - drying event (YZ, XZ, and XY planar views)
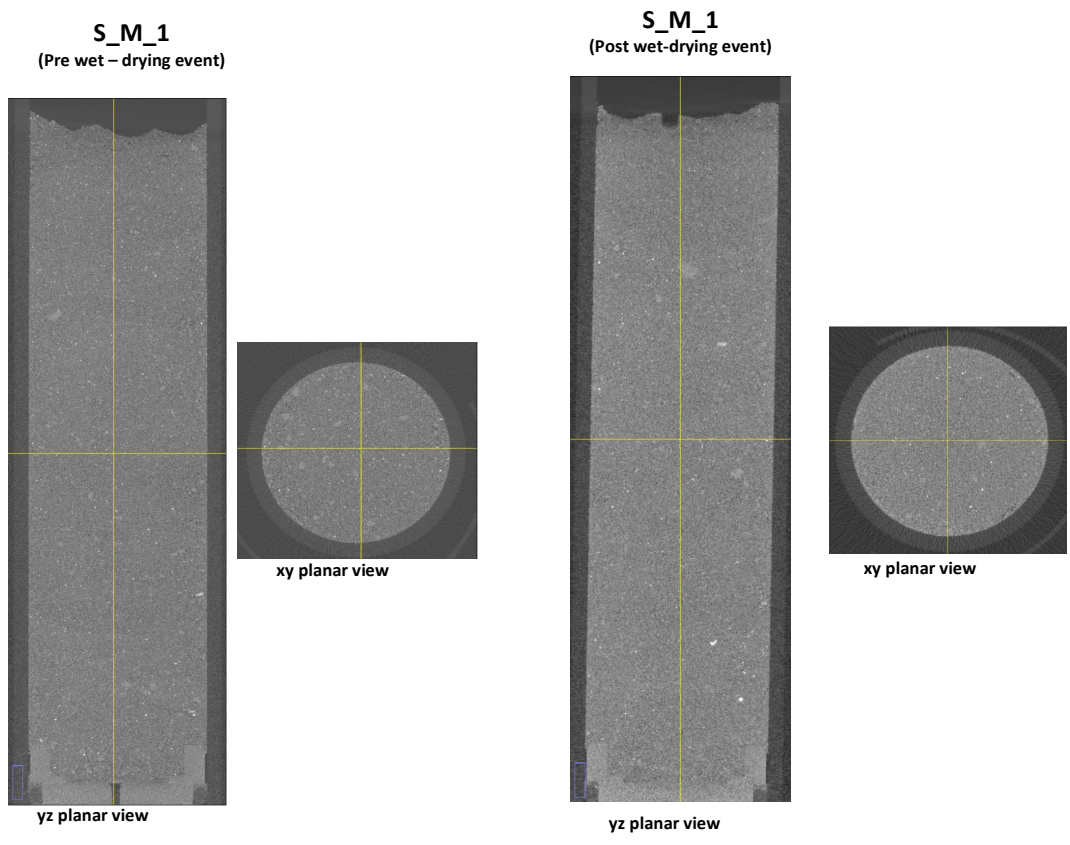
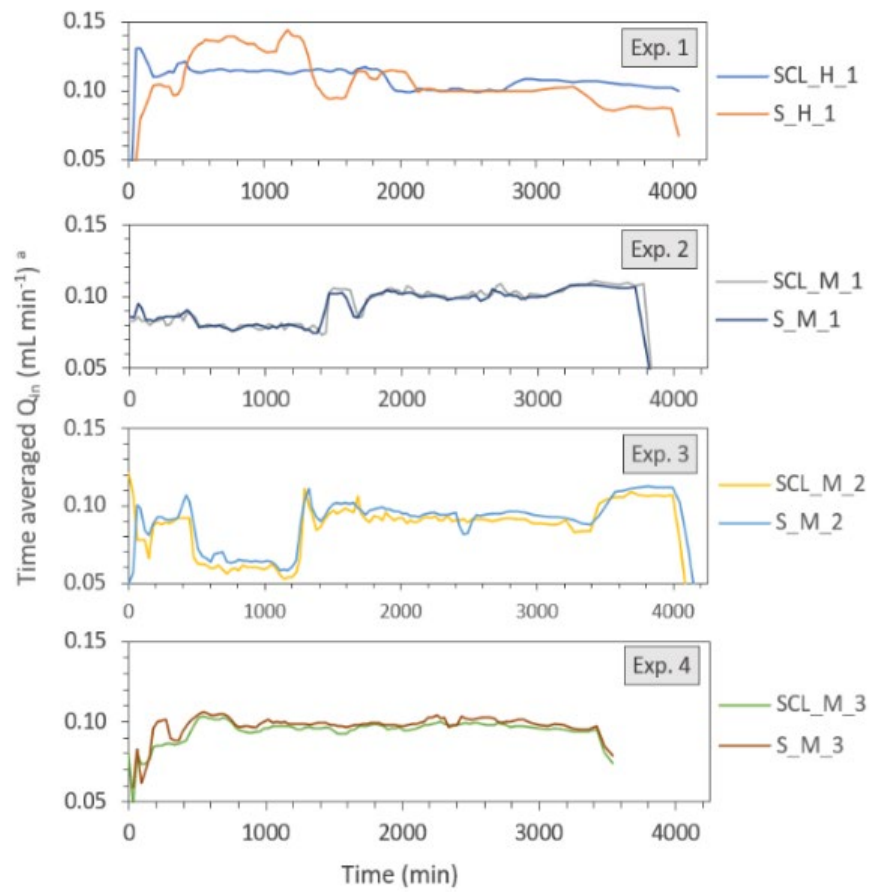Figure 25 Time-average volumetric flowrate (mL/min) for column flow

REFERENCES

1. Bodner, G., Leitner, D., & Kaul, H.-P. (**2014**). Coarse and fine root plants affect pore size distributions differently. *Plant and Soil*, *380*(1-2), 133–151. https://doi.org/10.1007/s11104-014-2079-8

2. C Corwin, D. L. (**2000**). Evaluation of a simple lysimeter-design modification to minimize sidewall flow. *Journal of Contaminant Hydrology*, *42*(1), 35–49. https://doi.org/10.1016/s0169-7722(99)00088-1

3. Demirkanli, D. I.; Molz, F. J.; Kaplan, D. I.; Fjeld, R. A. (**2009**). Soil-Root Interactions Controlling Upward Plutonium Transport in Variably Saturated Soils. *Vadose Zone Journal, 8*, (3), 574-585.

4. Demirkanli, D. I.; Molz, F. J.; Kaplan, D. I.; Fjeld, R. A., A fully transient model for long-term plutonium transport in the Savannah River Site vadose zone: Root water uptake. *Vadose Zone Journal* **2008,** *7*, (3), 1099-1109.

5. Demirkanli, D. I.; Molz, F. J.; Kaplan, D. I.; Fjeld, R. A.; Serkiz, S. M. (**2007**). Modeling long-term plutonium transport in the Savannah River Site vadose zone. *Vadose Zone Journal, 6*, (2), 344-353.

6. Edayilam, N., Ferguson, B., Montgomery, D., Al Mamun, A., Martinez, N., Powell, B. A., & Tharayil, N. (**2020**). Dissolution and vertical transport of uranium from stable mineral forms by plants as influenced by the co-occurrence of uranium with phosphorus. *Environmental Science & Technology*, *54*(11), 6602–6609. https://doi.org/10.1021/acs.est.9b06559

7. Ghestem, M., Sidle, R. C., & Stokes, A. (**2011**). The influence of plant root systems on subsurface flow: Implications for slope stability. *BioScience*, *61*(11), 869–879. https://doi.org/10.1525/bio.2011.61.11.6

8. Hendrickx, J.M.H., and M. Flury. (**2001**). Uniform and preferential flow mechanisms in the vadose zone. In: Conceptual models of flow and transport in the fractured vadose zone. *Natl. Acad. Press*, Washington, DC. p. 149–187.

9. Hu, Q.-H., Weng, J.-Q., & Wang, J.-S. (**2010**). Sources of anthropogenic radionuclides in the environment: A Review. *Journal of Environmental Radioactivity*, *101*(6), 426–437. https://doi.org/10.1016/j.jenvrad.2008.08.004

10. Kaplan, D. I., Smith, R., Parker, C. J., Baker, M., Cabrera, T., Ferguson, B. O., Kemner, K. M., Laird, M., Logan, C., Lott, J., Manglass, L., Martinez, N. E., Montgomery, D., Seaman, J. C., Shapiro, M., & Powell, B. A. (**2020**). Uranium attenuated by a wetland 50 years after

release into a stream. *ACS Earth and Space Chemistry*, *4*(8), 1360–1366. https://doi.org/10.1021/acsearthspacechem.0c00124

11. Kaplan, D. I.; Powell, B.; Demirkanli, D. I.; Fjeld, R. A.; Molz, F. J.; Serkiz, S. M.; Coates, J. T., (**2004**). Influence of Oxidation States on Plutonium Mobility during Long-Term Transport through an Unsaturated Subsurface Environment. *Environmental Science and Technology, 38*, 5053-5058. https://doi.org/10.1021/es049406s

12. Lin P, et al. (**2017**). Plutonium partitioning behavior to humic acids from widely varying soils is related to carboxyl-containing organic compounds. *Environ. Sci. Technol.* 2017;51:11742–11751. https://doi.org/10.1021/acs.est.7b03409

13. Luo, S., Ku, T.-L., Roback, R., Murrell, M., & McLing, T. L. (**2000**). In-situ radionuclide transport and preferential groundwater flows at INEEL (Idaho): Decay-series disequilibrium studies. *Geochimica Et Cosmochimica Acta*, *64*(5), 867–881. https://doi.org/10.1016/s0016-7037(99)00373-7

14. Montgomery, D., Barber, K., Edayilam, N., Oqujiuba, K., Young, S., Biotidara, T., Gathers, A., Danjaji, M., Tharayil, N., Martinez, N., & Powell, B. (**2017**). The influence of citrate and oxalate on 99TCVII, CS, NPV and Uvi Sorption to a Savannah River Site soil. *Journal of Environmental Radioactivity*, *172*, 130–142. https://doi.org/10.1016/j.jenvrad.2017.03.017

15. Molz, F.; Demirkanli, I.; Thompson, S.; Kaplan, D. I.; Powell, B. A. (**2015**). Plutonium transport in soil and plants: An interdisciplinary study motivated by lysimeter experiments at the Savannah River Site. *Dynamics of fluids and transport in complex fractured-porous systems*, Co-publication: American Geophysical Union and John Wiley and Sons, Inc.: Washington DC and Hoboken, NJ, pp 183-208

16. Otosaka S, et al. (**2011**). Factors controlling mobility of (127)I and (129)I species in an acidic groundwater plume at the Savannah River Site. *Sci. Total Environ.* 409(19):3857–3865. https://doi.org/10.1016/j.scitotenv.2011.05.018

17. Pires LF, Auler AC, Roque WL, Mooney SJ. (**2020**). X-ray microtomography analysis of soil pore structure dynamics under wetting and drying cycles. *Geoderma*. 15;362:114103. https://doi.org/10.1016/j.geoderma.2019.114103

18. Powell, B. A., Kaplan, D. I., & Miller, T. M. (**2018**). Neptunium(V) sorption to vadose zone sediments: Reversible, not readily reducible, and predictable based on Fe-oxide content. *Chemical Geology*, *481*, 53–64. https://doi.org/10.1016/j.chemgeo.2018.01.026

19. Rousseau, J.P., J.R. Nimmo, S.R. Anderson, R.C. Bartholomay, L.L. Knobel, L.D. Cecil, E.R. Landa, G.P. Curtis, P.D. Glynn, K.G. Stollenwerk, E.M. Kwicklis, C.R. Bossong, and B.R. Orr. (**2004**). Review of the transport of selected radionuclides in the Interim Risk Assessment for the Radioactive Waste Management Complex, Waste Area Group 7, Operable Unit 7-

13/14, Idaho National Engineering and Environmental Laboratory, Idaho. USGS Water Resources Investigation Rep. (In press.) INEEL, Idaho Falls, ID.

20. U.S Department of Energy (DOE/NE-0088). "The History of Nuclear Energy". Office of Nuclear Energy, Science and Technology, Washington DC

21. U.S. Department of Energy, O. o. E. M. *Linking Legacies: Connecting the Cold War Nuclear Weapons Production Process to their Environmental Consequences*; DOE/EM-0319; United States Department of Energy: Washington, DC, 1997.

22. Sams, Allison C., "Geochemical Controls of Iodine Sorption to Wetland Sediments" (**2017**). All Theses. 2771. https://tigerprints.clemson.edu/all_theses/2771

23. Santschi, P., Quigg, A., Schwehr, K., & Xu, C. (**2019**). Experimental observations of radionuclide uptake by colloidal and particulate humic acids obtained from 14 soils collected worldwide. *Biological and Chemical Oceanography Data Management Office*. https://doi.org/10.1575/1912/bco-dmo.738833.1

24. Schlüter, S., Leuther, F., Vogler, S., and Vogel, H.-J. (**2016**). X-ray microtomography analysis of soil structure deformation caused by centrifugation, *Solid Earth*, 7, 129–140, https://doi.org/10.5194/se-7-129-2016

25. Seaman, J. C., & Roberts, K. A. (**2012**). Radionuclide fate and transport in terrestrial environments radionuclide. *Encyclopedia of Sustainability Science and Technology*, 8597–8634. https://doi.org/10.1007/978-1-4419-0851-3_281

26. Yan, L., Le, Q. V., Sonne, C., Yang, Y., Yang, H., Gu, H., Ma, L., Lam, S. S., & Peng, W. (**2021**). Phytoremediation of radionuclides in soil, sediments, and water. *Journal of Hazardous Materials*, *407*, 124771. https://doi.org/10.1016/j.jhazmat.2020.124771

27. Zachara, J. M., Long, P. E., Bargar, J., Davis, J. A., Fox, P., Fredrickson, J. K., Freshley, M. D., Konopka, A. E., Liu, C., McKinley, J. P., Rockhold, M. L., Williams, K. H., & Yabusaki, S. B. (**2013**). Persistence of uranium groundwater plumes: Contrasting mechanisms at two DOE sites in the groundwater–river interaction zone. *Journal of Contaminant Hydrology*, *147*, 45–72. https://doi.org/10.1016/j.jconhyd.2013.02.001

28. Office of Nuclear Energy. (2022, October 3). *5 fast facts about spent nuclear fuel*. Energy.gov. Retrieved October 24, 2022, from https://www.energy.gov/ne/articles/5-fast-facts-about-spent-nuclear-fuel#:~:text=If%20we%20take%20that%20a,spent%20fuel%20since%20the%201950s.

29. Hu, Q. H., Rose, T. P., Zavarin, M., Smith, D. K., Moran, J. E., & Zhao, P. H. (2008). Assessing field-scale migration of radionuclides at the Nevada Test Site: "mobile" species. *Journal of Environmental Radioactivity*, *99*(10), 1617–1630. https://doi.org/10.1016/j.jenvrad.2008.06.007

30. Hu, Q.-H., Weng, J.-Q., & Wang, J.-S. (2010). Sources of anthropogenic radionuclides in the environment: A Review. *Journal of Environmental Radioactivity*, *101*(6), 426–437. https://doi.org/10.1016/j.jenvrad.2008.08.004

31. Bondietti, E. A., & Francis, C. W. (1979). Geologic migration potentials of technetium-99 and neptunium-237. *Science*, *203*(4387), 1337–1340. https://doi.org/10.1126/science.203.4387.1337

32. Eckhardt, R. K. (2000). Yucca Mountain: Looking Ten Thousand Years into the Future. *Los Alamos Science*, *2*(26), 464–489.

33. Hendrickx, Jan M.H., and Markus Flury. "Uniform and Preferential Flow Mechanisms in the Vadose Zone." *National Academy of Sciences*, Jan. 2001, pp. 149–187., https://doi.org/https://doi.org/10.17226/10102

34. Van den Akker, J.J.H., and B. Soane. "Compaction." *Encyclopedia of Soils in the Environment*, Elsevier, Amsterdam, 2005, pp. 285–293.

35. United States, Dept. of Energy. *Facts from the Savannah River Site*, 20CC00295 ed., pp. 1–8.

36. "Programs - Waste Solidification." *SRS*, Dept. of Energy, 10 Feb. 2020, https://www.srs.gov/general/programs/solidification/index.htm

37. "Savannah River Site Waste Characterization." *U.S.NRC*, 12 July 2021, https://www.nrc.gov/waste/incidental-waste/wir-process/wir-locations/wir-srs.html

38. "MILabs Ultra-High Performance Synergistic Imaging" '*2022 Catalog*' Sep. 2022, https://www.milabs.com/download-brochure/

39. Van Genuchten, M. Th., and R. J. Wagenet. "Two-Site/Two-Region Models for Pesticide Transport and Degradation: Theoretical Development and Analytical Solutions." *Soil Science Society of America Journal*, vol. 53, no. 5, 1989, pp. 1303–1310., https://doi.org/10.2136/sssaj1989.03615995005300050001x

40. Padilla, Ingrid Y., et al. "The Effect of Water Content on Solute Transport in Unsaturated Porous Media." *Water Resources Research*, vol. 35, no. 11, Nov. 1999, pp. 3303–3313., https://doi.org/10.1029/1999wr900171

41. Dagan, G., and V. Cvetkovic. "Spatial Moments of a Kinetically Sorbing Solute Plume in a Heterogeneous Aquifer." *Water Resources Research*, vol. 29, no. 12, Dec. 1993, pp. 4053–4061., https://doi.org/10.1029/93wr02299

42. Ababou, R. "Approaches to Large Scale Unsaturated Flow in Heterogeneous, Stratified, and Fractured Geologic Media." *U.S.NRC*, , 1 Aug. 1991, https://doi.org/10.2172/138205

43. Blackmore, Sharon, et al. "Comparison of Unsaturated Flow and Solute Transport through Waste Rock at Two Experimental Scales Using Temporal Moments and Numerical Modeling." *Journal of Contaminant Hydrology*, vol. 171, Oct. 2014, pp. 49–65., https://doi.org/10.1016/j.jconhyd.2014.10.009

44. Brouyère, Serge. "Modelling the Migration of Contaminants through Variably Saturated Dual-Porosity, Dual-Permeability Chalk." *Journal of Contaminant Hydrology*, vol. 82, no. 3-4, Oct. 2006, pp. 195–219., https://doi.org/10.1016/j.jconhyd.2005.10.004

45. Kabala, Z. J., and G. Sposito, "A stochastic model of reactive solute transport with time-varying velocity in a heterogeneous aquifer", *Water Resour*. Res., 27(3), 341-350, 1991, https://doi-org.libproxy.clemson.edu/10.1029/90WR01906

46. Richards, L. A. "Capillary Conduction of Liquids through Porous Mediums." *AIP Publishing*, American Institute of Physics, 1 Jan. 1931, https://aip.scitation.org/doi/10.1063/1.1745010

47. Massabó, M., et al. "An Analytical Solution of the Advection Dispersion Equation in a Bounded Domain and Its Application to Laboratory Experiments." *Journal of Applied Mathematics*, vol. 2011, 2011, pp. 1–14., https://doi.org/10.1155/2011/493014

48. Mamun, Abdullah Al, "Characterization of Water Flow and Solute Transport Driven by Preferential Flow in Soil Vadose Zone" (2022). All Dissertations. 3010. https://tigerprints.clemson.edu/all_dissertations/3010?utm_source=tigerprints.clemson.edu%2Fall_dissertations%2F3010&utm_medium=PDF&utm_campaign=PDFCoverPages

49. Nkedi-Kizza, P., et al. "On the Equivalence of Two Conceptual Models for Describing Ion Exchange during Transport through an Aggregated Oxisol." *Water Resources Research*, vol. 20, no. 8, 1984, pp. 1123–1130., https://doi.org/10.1029/wr020i008p01123

50. Toride, Nobuo, et al. "A Comprehensive Set of Analytical Solutions for Nonequilibrium Solute Transport with First-Order Decay and Zero-Order Production." *Water Resources Research*, vol. 29, no. 7, 1993, pp. 2167–2182., https://doi.org/10.1029/93wr00496

51. Folger, Scott. "Distribution of Residence Time for Chemical Reactors." *Elements of Chemical Reaction Engineering*, 4th ed., Pearson Education Internat, Upper Saddle River, NJ, 2006, pp. 867–900.

52. Wilmarth, William R., et al. "Review: Waste-Pretreatment Technologies for Remediation of Legacy Defense Nuclear Wastes." *Solvent Extraction and Ion Exchange*, vol. 29, no. 1, 2011, pp. 1–48., https://doi.org/10.1080/07366299.2011.539134

53. Montgomery, D.; Barber, K.; Edayilam, N.; Oqujiuba, K.; Young, S.; Biotidara, T.; Gathers, A.; Danjaji, M.; Tharayil, N.; Martinez, N.; Powell, B., The influence of citrate and oxalate on 99TcVII, Cs, NpV and UVI sorption to a Savannah River Site soil. *Journal of Environmental Radioactivity* **2017,** *172*, 130-142.

54. Powell, B. A.; Kaplan, D. I.; Miller, T., Neptunium(V) sorption to vadose zone sediments: Reversible, not readily reducible, and predictable based on Fe-oxide content. *Chem. Geol.* **2018,** *481*, 53-64.

55. Peruski, K. M.; Maloubier, M.; Kaplan, D. I.; Almond, P. M.; Powell, B. A., Mobility of Aqueous and Colloidal Neptunium Species in Field Lysimeter Experiments. *Environmental Science & Technology* **2018,** *52* (4), 1963-1970.

56. "Historical Conditions for Aiken County." *Standardized Precipitation Index*, National Oceanic and Atmospheric Administration's (NOAA) National Centers for Environmental Information (NCEI), 1 Jan. 2023, https://www.drought.gov/location/29801%2C%20Aiken%2C%20South%20Carolina. Accessed 11 Nov. 2023.

57. Powell, B. A., Kaplan, D. I., & Miller, T. M. (2018). Neptunium(V) sorption to vadose zone sediments: Reversible, not readily reducible, and predictable based on Fe-oxide content. Chemical Geology, 481, 53–64. https://doi.org/10.1016/j.chemgeo.2018.01.026

58. Luo, Shangde, et al. "In-Situ Radionuclide Transport and Preferential Groundwater Flows at INEEL (Idaho): Decay-Series Disequilibrium Studies." *Geochimica Et Cosmochimica Acta*, vol. 64, no. 5, 2000, pp. 867–881., https://doi.org/10.1016/s0016-7037(99)00373-7.

59. Bundt, Maya, et al. "Impact of Preferential Flow on Radionuclide Distribution in Soil." *Environmental Science & Technology*, vol. 34, no. 18, 2000, pp. 3895–3899., https://doi.org/10.1021/es9913636.

60. Moradi, Ghazal, and Behrouz Mehdinejadiani. "An Experimental Study on Scale Dependency of Fractional Dispersion Coefficient." *Arabian Journal of Geosciences*, vol. 13, no. 11, 2020, https://doi.org/10.1007/s12517-020-05438-z.

61. Zhang, Yinghu, et al. "A Review of Preferential Water Flow in Soil Science." *Canadian Journal of Soil Science*, vol. 98, no. 4, 2018, pp. 604–618., https://doi.org/10.1139/cjss-2018-0046.

62. Stumpp, Christine, and Gerhard Kammerer. "The Vadose Zone—a Semi-Aquatic Ecosystem." *Encyclopedia of Inland Waters*, 2022, pp. 331–338., https://doi.org/10.1016/b978-0-12-819166-8.00179-1.

63. Shook, Michael G. "Tracer Interpretation Using Temporal Moments on a Spreadsheet." *INL/EXT-05-00400*, 2005, https://doi.org/10.2172/910998.